Sofia University "St. Kliment Ohridski"
Faculty of Chemistry and Pharmacy
Department of Physicochemistry

Dimitar Nikolaev Shandurkov

SPECTRAL AND PHYSICOCHEMICAL PROPERTIES OF AEROGEL COMPOSITES

Abstract

to the thesis for the award of the degree of Doctor of Education and Science in the scientific specialty 4.2 - Chemistry - Physicochemistry

Supervisor: Prof. Dr. Stoyan Ivanov Gutsov

Sofia
2024

Contents

4.2.1. Preparation.

4.2.2 UV-Vis-NIR spectra in diffuse reflection mode.

4.2.3. Emission and excitation spectra. Quantum yield.

5. Conclusions.

6. Contributions to the thesis.

7. Publications including results of the dissertation.

8. Participation with papers at conferences including results of the dissertation.

9. Citations of publications included in the dissertation.

10. References used.

1. Introduction.

We identify the development of materials and technology as the greatest driver in human history. Although the development of modern materials science began in the late nineteenth and early twentieth centuries, the eras in history bear the names of the materials most used in their respective periods. The first tools and tools made were from materials that could be easily found directly in nature - stones, clay, wood and bone. The oldest tools found are made of flint and are estimated to be about 300,000 years old. The first development in materials science was the development of new technologies for processing materials. This opened up the possibility of using other stones for tools and making stronger and sharper stone axes. Together with this new knowledge and skills, combined with human creativity and complex relationships, led to the emergence of the first artists - 'painters' and 'jewellers'. The oldest paintings preserved in caves have been dated to 50,000 years old, and the most ancient jewelry and ornaments have been estimated to be 30,000 years old and are made from a variety of clays, ceramics and stones. For pigments, crushed materials that can be found in nature or easily made such as red and yellow ochre, hematite manganese oxide and charcoal were used. The first major development in technology came when people began to use fire to process materials, not just for heating, cooking and lighting. The introduction of thermal methods into materials science opened the door to the first potters. The earliest pottery vessels and figurines have been found in Japan and are estimated to be around 16 500 years old. The next great leap in the development of materials and technology came when we discovered that, after heat treatment, certain rocks and minerals yielded metals. The first metal we obtain and use en masse to make tools is copper. It appears around 6000 years before Christ.

The following millennia saw the discovery and development of various alloys of copper and tin, generally called bronze. Different alloys were used in different regions with different ratios of the two metals and different alloying additives depending, above all, on the availability in the surroundings and the purpose for which the respective tools were used. The advent of these new materials not only facilitated hunting, waterfowling and farming by creating stronger and more reliable tools, weapons, armour and implements, but also gave great development to medicine. Then medical instruments were created knives, scalpels, spikes and others, which in form and function very much resembled modern ones. The oldest refractories are composite bricks and asbestos-based fabrics made by the ancient Greeks. The first glasses were obtained 12 000 years ago in the Near East. Nine centuries later in the Roman Republic, methods for obtaining and processing glass were strongly developed. It was there that the methods of glassblowing and the use of moulds to produce different final shapes were first developed. Modern clear soda glass was first made in the mid-15th century, and the first glass optical lenses did not appear until the late 16th century in the Netherlands. They allowed us for the first time to observe small objects as well as to study the surrounding cosmos. The earliest window panes were made by pouring molten glass onto slabs of clay or sand. In the 3rd century BC, iron was first made. A few centuries after that, methods began to develop for making steel by using coal in special furnaces. In the modern era, methods for obtaining new materials and new techniques for processing them were mainly

developed. Casting, forging and cold working of softer metals developed. Over the centuries, a variety of furnaces were developed for smelting metals. From a closed type - a trench covered with clay or earth, the first furnaces were made in the Middle Ages that relied on blowing air. The method of processing and preparation was found to have a great influence on the final properties of the metal product. Foundry alloys proved suitable for structural purposes, while wrought metals and alloys such as Damascus steel were used primarily for weapons and swords. Methods have been discovered for producing coloured glass and glazing ceramics. As civilizations developed, ever larger settlements - cities and later entire megacities - appeared. Building them was a major infrastructural challenge. Housing and outbuildings were constructed from a variety of stones, wood, metal and bricks made from clays and ceramics. A very important aspect for the maintenance of these settlements was the water supply. The first pipes to carry water over long distances were made of spliced ceramic segments and easy to work metals such as lead. Now, metal pipes or those made of synthetic polymers are most commonly used. Late in the 1700s the first copper-zinc battery was described. In the XIX the vulcanized rubber, thermite mixture welding and the first photographs were discovered. Throughout most of human history, individual discoveries have remained used mainly locally. Much knowledge has not spread for cultural and economic reasons, but mostly because of the difficulties of transmitting information over great distances. For a very long time, paper and the pigments with which things could be depicted on it remained too expensive for widespread use. The development of digital media solves these problems. The advent of magnetic media such as cassettes and diskettes greatly increases the density of information that can be stored and transmitted. Modern optical, magnetic and semiconductor storage devices allow the handling of colossal amounts of information containing not only text and images but also various sounds, instructions and programs. Information transfer has also evolved with advances in materials and technology. From oral transmission, to postal services, to telegraphs and modern electrical and fibre optic cables, which can now carry information in real time to virtually anywhere on Earth.

The empirical and alchemical methods that have been used before have brought much knowledge from the Stone Age to the present, but the lack of a system for analyzing the results has prevented the rapid development of new technologies and materials. The end of the 19th and the beginning of the 20th century saw the first institutions whose purpose was to systematize and generalize the knowledge and information obtained. Many universities and institutes set up various departments and chairs to deal with a particular class of materials. With the development of mathematics, chemistry and physics, the first theoretical tools were created to give a description of the observed results. This opened the door to a better understanding of nature and its laws, which greatly accelerated scientific progress in the last century. For the first time, in the past twentieth century, theoretical development overtook empirical material science. The search for theories to explain observed physical phenomena led to the development of two of the most significant theories in human history, Relativity Theory and Quantum Mechanics. The development of physics and chemistry, as well as computing, allows not only the description but also the prediction of a number of properties of materials that have not yet been derived and investigated. The discovery of semiconductor materials has proved so significant that the age in which we now live is named after one such material, silicon. The optimum use of this type of material would be impossible without the theoretical knowledge we have. Quantum mechanics has helped to

conceptualize, obtain, and study a vast number of materials without which our lives would take a very different form-semiconductors, liquid crystals, luminescent materials, and others. They gave rise to modern computing, which now finds applications in every aspect of our daily lives - phones and computers, control systems and sensors.

The knowledge of different metals and their properties has allowed the creation of a huge number of alloys for all sorts of applications. Strong alloys for construction, high-strength steels and alloys to withstand heavy loads, chemical resistant materials for the chemical and food industries and corrosion resistant steels for shipbuilding. The development of lightweight aluminium and titanium alloys and composites is displacing wood as the main material in aircraft construction. The beginning of the 20th century saw the first synthetic polymer, Bakelite. Plastics proved to be cheap, easy to produce and usually much lighter than metals. This allowed commercialisation and the emergence of many new products. Ceramics and glasses have been developed with applications in a variety of fields. From building materials to refractory bricks for furnace construction, porous ceramics for thermal and acoustic insulation, electrical insulators on small electrical components and large electrical transmission equipment and ceramics with luminescent properties finding use in lighting.

Modern materials are succeeding in radically changing the way we light ourselves. The burning of animal and vegetable fat in ceramic lamps, the burning of liquid hydrocarbons and the use of candles has long since been superseded by light bulbs (heated metal wire in an inert atmosphere), metal vapour lamps (sodium, mercury vapour), metal halide lamps, gas discharge lamps (noble gases, deuterium, etc.), LED materials, luminescent materials, quantum dots and many others. Our accumulated knowledge of chemistry and physics also allows us to control the colour of the emitted light. This has produced coloured lamps and displays capable of producing millions of different colours.

This dissertation focuses on a particular class of materials - luminescent composites. Composite materials are a class of materials that is a combination of at least two others with fundamentally different properties. Unlike mixtures and solutions, in composite materials, the different components remain phase separated. Examples of widely used synthetic composite materials are reinforced concrete, automobile tires, glass fiber reinforced plastics and alloys, plywood. Various composite materials such as wood and animal bones are also found in nature. These combine a rigid component, cellulose or hydroxyapatite, with a soft and flexible polymer, lignin, in plants and collagen, in animals.

Composite materials can also be viewed as frozen dispersions (solid colloidal solutions), where the dispersed phase can be micro- or nano-sized, in the form of fibres or layers, as opposed to solid solutions where the dopant is dispersed at the molecular level. Control of the chemical composition and microstructure of the dispersed phase becomes a lever for developing the functionality of the composites.

For the purpose of this thesis, hybrid composites based on silicate aerogels and the luminescent complexes bis-phenanthroline europium trinitrate [Eu(phen)2](NO3)3 and bis-phenanthroline terbium trinitrate [Tb(phen)2](NO3)3 were prepared. The main objective is to obtain materials that

combine the chemical resistance of silicates, the low thermal conductivity of aerogels and provide a matrix that protects the luminescent components from environmental influences such as moisture, temperature and various mechanical effects.

Aerogels are a very broad and well-studied class of compounds for thermal, acoustic and electrical insulation, but their high porosity allows other components to be incorporated into their pores. The luminescent properties of europium and terbium ions have been extensively studied and described. Many hybrid complexes, ceramics and glasses doped with these elements are known to have luminescent properties. Most research has focused on pure luminescent components or their solutions. The compounds and properties of rare earth ions with 1,10-phenanthroline as well as a number of its derivatives have been described in detail. These particular complex compounds have been chosen because of their ease of preparation. Their low solubility in water and ethanol allows them to be prepared by minimal chemical preparation. Mixing solutions of the rare-earth ions and the ligand 1,10-phenanthroline leads to the rapid precipitation of microcrystallites of the corresponding lanthanide complexes. This is exactly what Gutsov et al. used when they first prepared in situ and described this class of composite materials.

This dissertation develops questions related to the property-structure relationship of aerogel granules containing rare earth ion complexes with phenanthroline, focusing on the influence of the matrix on the luminescent properties of the composite materials. A series of silica aerogel matrices with different degrees of hydrophobicity were synthesized. For the first time, a spectroscopic methodology was developed to investigate the hydrophobicity of bulk silica materials and the textural properties of the different matrices were characterized by physical methods. A new more efficient methodology for functionalization of aerogel beads was obtained and two series were made: the different matrices doped with europium and with terbium complex. The photophysical properties of the resulting luminescent composites are investigated in detail and described as a function of the degree of hydrophobicity of the matrix.

Subsequent chapters will provide readers with detailed information on the properties, development, and various methods for the preparation and characterization of silicate aerogel materials. Physical methods for analyzing the porosity of the materials are discussed and it is shown how maximum information can be extracted from them - specific surface area, pore size distribution, texture study, morphology and shape of the pores as well as surface fractal coefficients of the surface of the gels. The basic luminescence properties of europium and terbium ions are shown. The theoretical foundations of the photophysical processes of absorption and emission of light (electromagnetic radiation in the frequency range 1012-1016 Hz) are given. It is shown how structural analysis can be performed by spectroscopic methods. The experimental procedures, results and detailed interpretation of all the data obtained are then outlined. X-ray structural analysis is used to confirm the spectroscopic structural studies. It turns out that the hydrophobicity of the matrix strongly influences the limiting properties of the embedded hybrid complexes in the pores of the gels. The developed methodology proves to be highly suitable for "tuning" the quantum yield and emission color of the materials. Materials with quantum yields as high as 35% and multicolor emission were obtained. In the future, this may lead to new standards for measuring low quantum yields, luminaires with fewer components or different sensors.

2. Aims and objectives of the dissertation.

The main objectives of this thesis are to find a reproducible method for the synthesis, hydrophobization and functionalization of silicate aerogel granules and to investigate the dependence of their textural and spectral properties on the degree of hydrophobization. The obtained systems are a series of porous amorphous SiO2 with different degrees of hydrophobicity and hybrid composites based on them with the complexes [Eu(phen)2](NO3)3 and [Tb(phen)2](NO3)3.

To fulfill these objectives, the following tasks were set:

- To find a reproducible physicochemical method for the preparation and hydrophobization of silicate aerogel granules.

- Characterization of the silicate matrix by IR spectroscopy and low temperature absorption and desorption isotherms.

- Development of a methodology for the preparation of hybrid composites based on SiO2:[Eu(phen)2](NO3)3 and SiO2:[Tb(phen)2](NO3)3.

- Detailed study and description of the spectral properties of the obtained composites by means of diffuse reflection spectra and emission and excitation spectra.

- Investigation of the influence of matrix hydrophobicity on the quantum yield of the resulting composites.

- Investigation of the microstructure of the obtained nanocomposites by diffraction and microscopic methods.

3. Literature Review

3.1. Aerogel materials.

3.1.1 Preparation methods.

The first successfully synthesized aerogel was obtained by Kistler in the early 1930s. Together with his collaborators, he manages to dry wet silica gel without destroying its pore structure, which would lead to shrinkage and cracking. For this purpose, a supercritical drying method for the samples has been developed. Another important discovery they make is the possibility of changing the solvent in the wet gel. The condition for replacing one solvent with another is that the two liquids must be miscible with each other. Otherwise, a phase boundary forms between the two liquids, creating stresses in the matrix that could lead to the destruction of the porous structure of the gel. The correct selection of solvent facilitates the drying of the sample and allows the process to be conducted at lower temperatures and pressures. Kistler successfully applies this process and obtains aerogels not only from SiO2 and Al2O3 but also from nickel tartrate, tin oxide, tungsten oxide, gelatin, agar, cellulose, nitrocellulose, and egg albumin.

With this, Kistler initiated a new class of functional materials that continues to evolve to this day. Soon after Kistler's publications, many other authors and research teams managed to obtain various aerogels. Teichner and co-authors manage to synthesize a variety of silicate aerogels, as well as different oxide and mixed oxide gels [3,4]. At Sandia National Laboratories, the first boron aerogels are obtained, while Pekala creates the first resorcinol-formaldehyde aerogel, which, upon pyrolysis, carbonizes into a carbon gel that is electrically conductive. Silicate gels are most commonly obtained using the sol-gel method through the hydrolysis of various silicon alkoxides. The process goes through two main reactions, namely, the hydrolysis of the alkoxide and the polycondensation of partially or fully hydrolyzed species. The reaction of hydrolysis occurs as a nucleophilic substitution of the alkoxide group.

$$\equiv Si - OR + H - OH \rightarrow \equiv Si - OH + HOR \quad (1)$$

An oxygen atom from a water molecule or a hydroxyl group attacks the partially positively charged silicon atom (δ+Si=0.32 for TEOS) [9], resulting in the departure of an alcohol molecule and the formation of a silanol group (Si-OH), which can participate in a condensation reaction with another Si-OH or Si-OR group.

$$\equiv Si - OH + HO - Si \equiv \rightarrow \equiv Si - O - Si \equiv + HOH \quad (2)$$

$$\equiv Si - OR + HO - Si \equiv \rightarrow \equiv Si - O - Si \equiv + HOR \quad (3)$$

In the polycondensation reaction, a siloxane bridge (Si-O-Si) and a low-molecular-weight product – water or alcohol – are formed. It is precisely this process that leads to the formation of silicate oligomers. At the same time, the viscosity of the ash increases until the oligomers or individual particles bond with each other and form a gel. During the gelation process, a sharp increase in the viscosity of the system is observed. The reactions of hydrolysis and condensation are usually catalyzed by mineral acids, bases, ammonia, acetic acid, or fluorides. The speed of reactions is strongly influenced by the pH of the medium, the molar ratio of water to precursor, temperature, solvent, as well as the precursor itself. The reaction of hydrolysis of TEOS can be viewed as a thermally activated Arrhenius process. Kinetic experiments show that the apparent

activation energy of its hydrolysis is 36.4 kJ/mol. Usually, in an acidic environment, the hydrolysis reaction is favored and its rate is higher than that of the polycondensation reaction [3,10–15]. In this way, gels are obtained with a morphology closer to that of organic polymer gels. On the other hand, in an alkaline environment, the condensation reaction occurs at a faster rate [15–17]. This is how silicate particles are formed, which can subsequently agglomerate to produce a colloidal gel [8].

An important step before drying the gel is its maturation. (aging). During the aging of the gel, the reactions of hydrolysis and polycondensation are completed. The gel densifies, the average size of its pores increases, and its mechanical properties improve. The maturation of the gel can be facilitated by adding water and/or additional monomer units (TEOS), which can react with non-hydrolyzed alkoxide groups or Si-OH groups [11,18]. The maturation of gels utilizes the phenomena of syneresis and Ostwald ripening by altering the composition of the liquid phase of the wet gel. As a result, additional polycondensation reactions occur, involving unreacted hydroxyl groups from the surface of the gel. It is possible to observe processes of dissolution and precipitation of silicate particles. These processes lead to an increase in apparent density and the average diameter of the pores. The speed strongly depends on the pH and the type of solvents used. Research shows that the physical properties such as hardness, elastic modulus, shear modulus, thermal capacity, and others increase [8]. After the gel has matured, a number of surface modifications can be carried out, which will be discussed in the next section.

One of the most important stages in obtaining aerogels is their drying. The goal is to remove the solvent from the pores without destroying them. The presence of a liquid-gas meniscus in the pores of the gel inevitably leads to strong mechanical stresses, which can result in the destruction of the gel's porous structure. To obtain an aerogel, the drying process must be conducted in such a way that minimal structural changes occur—such as breakages and shrinkages of the sample. The solvent can be removed by transitioning to a gaseous or supercritical state. Three main drying methods have been developed based on the phase transition that occurs. Figure 2 shows the phase diagram of a single-component system.

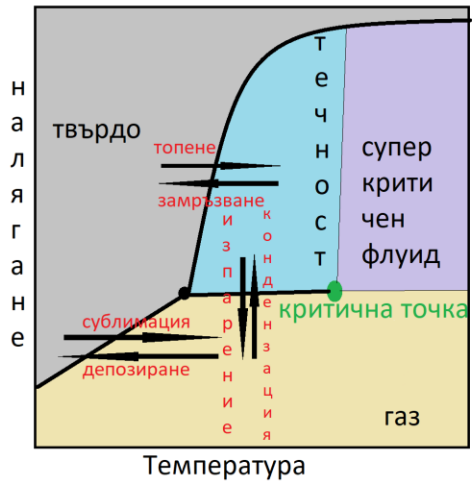

Fig. 2. Phase diagram of one component system.

From the diagram, it can be concluded that there are three main methods for drying gels:
• Freeze-drying – drying by freezing and sublimation of the solvent.
• Evaporation drying of the solvent (transition from liquid-gas equilibrium)
• Supercritical drying, aimed at achieving supercritical pressure and temperature.

Subcritical drying methods remain the most commonly used for obtaining aerogel samples. They allow drying to be carried out at room temperature, under vacuum, or at atmospheric pressure, resulting in large quantities of powders and granules. The capillary tensions in the pores of the gel depend on the surface tension, the viscosity of the solvent in the pores, and the permeability of the gel.

3.1.2 Surface modification of aerogel materials.

The addition of various agents controlling drying (Drying Control Chemical Additives) can affect the pore size of the resulting gel. Substances such as polyvinyl alcohol (PVA), polyethylene glycol (PEG), glycerin, and various surfactants can reduce the stresses during the evaporation of the solvent from the pores [8]. Water molecules can form strong hydrogen bonds with unreacted –OH groups on the surface of the gel, leading to strong water adsorption by hydrophilic silica gels. Some types are even hygroscopic. It has been observed that in a humid environment, such gels can absorb large amounts of water, resulting in cloudiness, cracking, and breaking, which significantly deteriorates their mechanical and insulating properties. Such a gel is no longer suitable for a matrix in composite material, as it does not provide good protection against external influences such as moisture and temperature changes [8]. Hydrophobization is an effective method for surface modification by adding groups that do not participate in the hydrolysis reaction. This can be achieved by using silicate precursors with a non-hydrolyzable group or by silanizing the already prepared gel. In this way, hydrophobic samples are obtained.

Other authors show that the gel can be hydrophobized even after it has been obtained. Gels can be treated with agents such as hexamethyldisilazane [19] or trimethylchlorosilane (TMCS) [20–22]. These substances react exothermically with hydroxyl groups on the surface of the gel and replace them with hydrophobic –Si(CH3)3 groups.

When the gel is silanized before being dried, the wetting angle in the pores changes, which in turn reduces the capillary tensions. When drying silanized gel, the so-called spring effect is observed, in which the pores fully or partially regain their shape and volume after the solvent leaves the pores [8].

3.1.3 Physicochemical properties.

Aerogels are distinguished by their remarkable physicochemical properties. The density of the skeleton of silica gels is close to that of bulk silicon dioxide (2.2 g/cm3), but due to their high porosity, aerogels are the materials with the lowest density known to us (0.001-0.5 g/cm3) [8,23,24]. Usually, the volumetric portion of the pores is over 95% of the volume of the monolith, and most often, aerogels fall into the mesoporous materials category, meaning that the pore

diameter ranges between 5 and 100 nm. This class of materials is also characterized by its exceptionally well-developed specific surface area of 250-800 m²/g, but there are also those with a specific surface area of more than 1000 m²/g [8,13,25,26].

Aerogels have very low thermal conductivity. At standard temperature and pressure (STP), it is about 0.02 W/mK and is lower than that of air – 0.025 W/mK [27–29]. This makes them some of the best insulating materials. The thermal conductivity λ of a material can be expressed with the following formula:

$$\lambda = C_p \rho L_p < v_p >, \quad [5]$$

Where Cp is the heat capacity, ρ is the density of the gel, Lp is the average free path of the phonons, and is the average speed of the phonons. Nanopores lead to a decrease in the average free path of gas molecules. In addition to their low density and interesting thermal properties, aerogels have a low refractive index (1.002), a low speed of sound (100 m/s), and a low dielectric constant (1.008 for 3-40 GHz) [8].

3.2 Aerogel composite materials, containing lanthanide complexes.

3.2.1 Functionalization of aerogel granules and powders.

One of the first articles related to aerogel composites with lanthanide complexes is by S. Gutzov et al, [21]. The difference with sol-gel composites is the possibility of functionalizing the silicate powders after their production, their low density, high porosity, and the presence of a huge specific surface area. A method for impregnation has been proposed that directly replicates what is known from classical sol-gel systems with low porosity [21,25,26]. In this first study, open questions remain, such as the volumes of the dopant solution, the influence of the matrix and the photophysical characteristics of the composites, as well as the effect of the degree of hydrophobization of the matrix on the quantum yield and the decay times of luminescence. Several compositions have been examined, focusing on the influence of the activator concentration on the spectrum, following the logic of "concentration quenching" in phosphors [30].

These questions are part of those discussed in the dissertation. Ако погледнем класическите зол-гелни материали, основният метод за получаване на композити е методът на импрегнирането с разтвор на лантанидини йони. At the same time, work is conducted with very low concentrations, relying on equilibrium adsorption isotherms. From 2012 to 2014, the Functional Optical Materials group developed an in situ doping method, a two-stage process used for europium complexes.

3.3 Spectral methods for characterizing oxide sol-gel materials.

3.3.1 Infrared spectroscopy..

Infrared (IR) or vibrational spectroscopy studies the interactions of the infrared part of the electromagnetic spectrum with matter. These interactions can be absorption, emission, or reflection. The infrared region roughly encompasses electromagnetic radiations with energy

ranging from 10 to 14,000 cm-1 and can be conventionally divided into three parts. In the far infrared region (10-400 cm-1), high-energy molecular rotations and low-energy molecular vibrations and lattice vibrations are observed. The average IR region encompasses the range of 400-4000 cm-1, where the characteristic molecular vibrations are found. This field finds the widest application in chemical analyses due to the relatively simple experimental techniques, easy sample preparation, and clear interpretation of the spectra of many functional groups. It allows for the analysis of known and unknown chemical compounds and mixtures, the determination of the presence of various functional groups in materials, and the investigation of the structure and bonding in polymers, ceramics, and glass [31,32]. Various experimental techniques allow for the determination of porosity and the arrangement of structural elements in oxide gels, glasses, and ceramics. The last region of the infrared spectrum is the near-infrared region, which is located in the range of 4000-14000 cm-1. There are various overtones and combination vibrations of the molecules observed there. The presence of combination vibrations makes the analysis of spectra in the near-infrared region difficult. This method proves to be particularly suitable for samples with a known composition. This makes it easier to determine the origin of the stripes. Near-infrared spectroscopy allows for the rapid identification of various solvents in the sample [31–33].

In IR spectroscopy, only transitions that lead to a change in the dipole moment of the molecule are observed. With a greater change in the dipole moment due to the corresponding vibration, a larger relative intensity of the respective transition in the IR spectrum of the molecule is expected. Transitions that lead to a change in the polarizability of the molecule are active in Raman spectroscopy. Analyzing the symmetry of the studied molecule and placing it in a specific symmetry group can facilitate the analysis of vibrational and spectral data. There are reference guides created that outline each symmetry group, the number of allowed transitions, the number of degenerate states, and which are IR and Raman active [32].

The peaks in IR spectroscopy do not appear as lines, but as bands with a certain width. This is due to anharmonic effects and inhomogeneous broadening. Theoretically, IR bands are well described by Lorentzian curves; however, in many cases, the profile changes due to the characteristics of the optical system of the spectrometer and the superposition of multiple curves leading to a Gaussian or mixed profile [34].

3.3.2. Infrared spectroscopy of SiO_2. Central force model.

Silicon dioxide is composed of tetrahedra SiO4^2-, which arrange themselves into various structures – chains and rings. Additionally, uncondensed –OH groups and water molecules are present in the volume of the samples. The spectrum of amorphous silicon dioxide A-SiO2 (Fig. 9) has a number of bands due to the different structures in the material and residual water. The peak at 1631 cm-1 is due to the vibrations of water molecules, while the broad band at 3440 cm-1 corresponds to the stretching of the O-H bond. The vibrations at 466, 620, and 800 cm-1 are symmetric and antisymmetric vibrations of the tetrahedra and hydroxyl groups [35–42]. The broad peak at 1000-1250 cm-1 includes energy-close vibrations of silicon dioxide. Chemical groups are observed in glasses in different chemical environments. Amorphous materials lack translational symmetry because there are differences in the lengths of chemical bonds and the

valence angles between the structural elements that make them up. This leads to the convolution of strips from many closely positioned peaks. In spectroscopy, this is referred to as inhomogeneous broadening of the lines, and it is very pronounced in the spectra of amorphous materials.

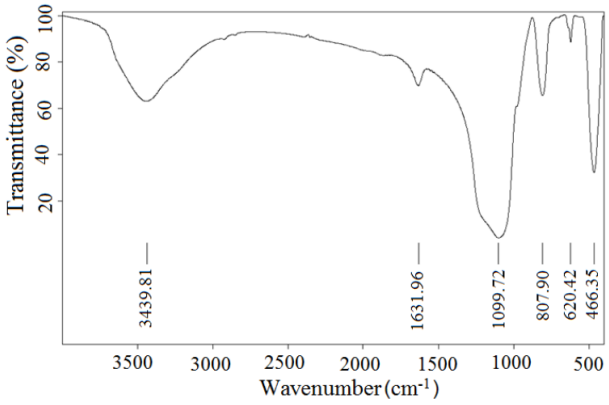

Fig. 9. IR spectrum of amourphous silica dioxide [35].

A number of authors create models to theoretically describe the spectra of glasses. One such model is the model of central forces applied to glasses with a structural element – tetrahedra AX4, such as silicon dioxide [39,43]. The broad peak at 1000-1250 cm-1 is interpreted as being composed of vibrations from various siloxane rings, primarily four-membered and six-membered rings, namely (Si-O)4 and (Si-O)6, as shown in Fig. 10 [42].

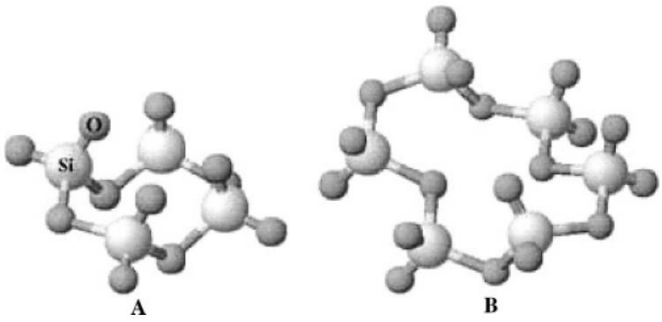

Fig. 10. A) Four membered siloxane rings and B) six membered siloxane rings.

The vibrations in a solid body can be divided into transverse and longitudinal. Transverse vibrations are vibrations perpendicular to the wave propagation vector, while longitudinal vibrations are parallel to it. There should be two transverse modes and one longitudinal mode. One of the widely used models for describing the IR spectra of silicon dioxide is the central force model by Sen and Thorpe, which only considers interactions between nearest neighbors and neglects long-range Coulomb interactions [36,39,43]. The model is very suitable for amorphous materials, where short-range order dominates.

The model of the central forces does not predict the splitting of the strip into two – for the transverse and longitudinal vibrations. The transverse vibrations shift towards 1050 cm-1, while the longitudinal ones are around 1200 cm-1. This leads to additional widening of the band, in relation to the spectrum of crystalline silicon dioxide – quartz [20,35,42].

3.3.3 Physical description of the processes of absorption and emission of light.

The processes of absorption and emission are physical processes of absorbing and releasing energy in the form of electromagnetic radiation. During the absorption of a photon, an electron from the activator moves to a higher energy level. This process is only possible when the energy of the electromagnetic radiation is equal to the difference in energies of the two energy levels ΔE.

$$\Delta E = E_2 - E_1 = h\vartheta \qquad (13)$$

E_1 – energy of ground state

E_2 – energy of excited state

h – Planck constant

ϑ – frequency of the electromagnetic radiation

The absorption and emission of electromagnetic radiation can be illustrated using a configuration coordinate diagram (E-R diagram) [30]. The configuration diagrams depict the potential energy of the absorbing center as a function of the configuration coordinate. The simplest model considers a stationary metal ion, with the ligands moving closer to or further away from it in phase. In this case, the diagram simplifies to two coordinates: E – potential energy and R – the distance between the ion and the ligand. The main drawback of this model is that it neglects the vibrations of the excited state. Figure 11 shows such a diagram. With g and e are marked the curves of the ground and excited states, respectively, while R0 and R0' are the equilibrium distances in the two states. The curves of the energy levels are parabolas because it is assumed that the vibrational motion is harmonic, meaning that Hooke's law is obeyed. The restoring force F is proportional to the displacement R from the equilibrium position R0.

$$F = -k(R - R_0) \qquad (14)$$

The curve of the excited state is once again described by a parabola, but it is usually shifted R0≠R0', because the two energy levels have different geometries due to changes in the chemical bonds [30]. The absorption process is most likely to begin from the minimum of the potential energy R=R0. It is precisely there that the maximum in the absorption spectrum is located. Absorption can also begin from R=R0±ΔR, albeit with a lower intensity; this process leads to the broadening of spectral lines. If R0=R0/, the two parabolas are located exactly one above the other. Then the width of the optical transition disappears, and the absorption becomes a narrow strip. This case very well describes the direct absorption of photons by the trivalent ions of the rare earth elements (4f elements) [51], and is referred to as the weak crystal field approximation. From the perspective of spectroscopy, this model is characterized by a very small Stokes shift, on the order of 50 – 200 cm-1, and indicates that the Hamiltonian of the crystal field HCF is significantly smaller than that of the spin-orbit interaction HSO, the electron-electron interaction HEE, and the interaction between the nucleus and the electrons H0.

The optical transitions in configuration-coordinate diagrams are referred to as vertical transitions. The reason is that vertical transitions in these diagrams are electronic, while

displacements along the horizontal axis correspond to the movement of atomic nuclei. Due to their greater mass, atomic nuclei move much more slowly than electrons, and it can be assumed that electronic transitions occur in a static environment [30], according to the Born-Oppenheimer approximation, and the transitions are single-electron. Not every possible electronic transition from the configuration-coordinate diagram is an allowed transition; selection rules are present [30] [66]:

- Spin selection rule – forbids transition between different spin states ($\Delta S \neq 0$).
- Parity selection rule – forbids transition between similar orbital types s-s, p-p, d-d. f-f преходи.

These rules arise from the conservation of angular momentum in a given process and the value of the spin of photons, which is equal to one. From here, it can be concluded that the total orbital angular momentum must change by $\Delta L=0, \pm 1$, while the total angular momentum can change by $\Delta J=0, \pm 1$, but transitions with $J=0 \leftrightarrow J=0$ are forbidden. Here, L, S, J are the designations from the Russell-Saunders scheme for labeling the electronic terms in multi-electron atoms.

Thanks to complex quantum physical effects and interactions caused by inhomogeneities in the matrix, these rules are not always followed in the solid state. The influence is exerted by spin-orbit interactions, electron-vibrational interactions, and asymmetric interactions with the crystal field, as well as the mixing of states with different J in Stark multiplets (J-mixing), leading to the lifting of quantum-mechanical restrictions [30,44,45].

In heavy atoms, spin-orbit interactions become comparable to or stronger than spin-spin interactions, which necessitates a different scheme for describing electronic levels and transitions. In this model, the quantum numbers S, L, and J do not provide a good description of the system's spin, and transitions with $\Delta S \neq 0$, for example between singlet and triplet levels, can be allowed. [46]

3.3.4 Absorption and emission from the ions Eu^{3+} и Tb^{3+}

The rare earth elements and their hybrid complexes are highly studied. In this dissertation, we have studied the complexes of the ions Eu3+ and Tb3+ due to their significant practical applications. The luminescent materials based on these ions are characterized by narrow and intense emission bands, which result in the production of bright and pure green and red colors. This is due to the weak splitting of the f-f lines. The optical properties of rare earth elements are determined by their partially filled 4f electron shell (4f0 for La3+ to 4f14 for Lu3+). He is well shielded by the filled 5s2 and 5p6 atomic orbitals. As a result, the matrix in which the ion is located has a very weak, but significant, influence on the configuration of the 4f orbitals. The electronic terms in lanthanide ions are described according to the Russell-Saunders scheme and are represented in the form (2S+1)LJ, where S is the total spin moment, 2S+1 is the multiplicity, L is the total orbital moment, and J is the total angular momentum [30,47–49].

The first described luminescent coordination compounds (complexes), in which a metal ion is surrounded by one or more organic molecules with electron-donor properties, were described

by Weissman in the 1940s, specifically in 1942. He observes that the absorption of light in the range of 320-440 nm by the organic component of the compound leads to the typical f-f emission bands of the Eu3+ ion. Studying a range of chelating agents such as beta-diketones, salicylates, benzoates, and picrates, Weissman concludes that the effectiveness of excitation is strongly influenced by the nature of the organic ligand, the solvent, and the temperature [50]. Now this process of energy transfer from the ligand to the activating ion is known as the "antenna effect" [51]. Crosby and co-authors demonstrate that the triplet state of the ligand has a strong influence on the energy transfer process [48,52,53].

Most lanthanide ions have luminescent properties. The intensity and color of the emitted radiation depend on the energy difference between the lowest excited state and the ground state. For the ions Eu3+ and Tb3+, the most intense transitions are 5D0→7F2 and 5D4→7F5, which correspond to the characteristic red and green colors of the emissions of the two ions, respectively. The transition energy for these ions is 12150 cm-1 and 14800 cm-1. Gd3+ has a very wide forbidden zone (32000 cm-1) and emits in the ultraviolet region of the electromagnetic spectrum, which is why its complexes are not used among luminescent materials. Dy and Sm emit yellow and orange light, while systems based on Nd, Ho, and Yb emit in the near-infrared region. In Fig. 12, the energy levels of luminescent lanthanide ions are schematically depicted, among which electronic transitions most commonly occur during the processes of absorption and emission of electromagnetic radiation [48].

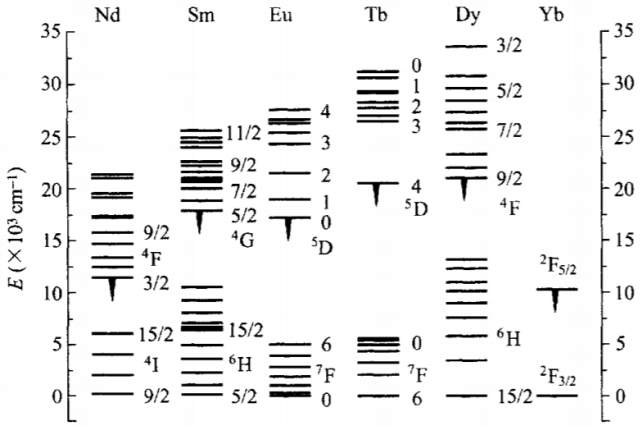

Fig. 12. Energy level diagram of some rare earth ions [48].

If the influence of temperature on the intensity of a given electronic transition is studied, it can be determined whether this transition is phonon-assisted. As the temperature decreases, the phonon energy of the matrix decreases, and consequently, the intensity of the corresponding electronic transition also decreases. Quantitative phonon-assisted (vibrational transitions) are described by the coth(x) model, a thermodynamic approximation derived from the phonon energy of crystals with temperature [54].

Direct excitation of f-f transitions rarely leads to intense luminescence; therefore, the antenna effect is used for the effective excitation of rare earth ions [48]. First, ultraviolet or blue photons are absorbed by the immediate surroundings of the activator (the organic ligands), causing them to transition into an excited singlet state, most commonly S1. Then, the organic molecules

relax to the lowest vibrational level of the excited singlet state, from where they can transition to the ground state through the process of fluorescence or move to the triplet state T1 via intersystem crossing. This transition is forbidden by spin, and therefore the triplet state has a long lifetime. From the triplet state, the ligand can transition to the ground state through phosphorescence or transfer its energy to the lanthanide ion [48]. Figure 13 schematically presents the antenna effect and the energy transfer in the Ln3+-ligand system. Quantum chemical calculations show that in some systems, higher triplet states of the organic ligand also have an influence [55]

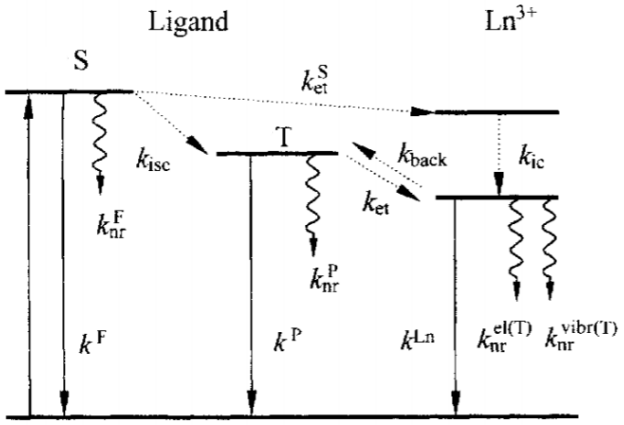

Fig. 13. Antenna effect and energy transfer from the ligand to the activator. S - excited singlet state, T - triplet state of the ligand, F – fluorescence, P – phosphorescence [48].

There are two main mechanisms known for the transfer of energy from the triplet state of the chromophore to the activator ion. The first, known as the Dexter mechanism or the exchange mechanism, involves the exchange of two electrons. After the excitation of an electron to the first singlet state of the ligand and intersystem crossing to the triplet state, this electron jumps to one of the excited levels of the activator, while an electron from the ground state of the activator jumps to the ligand to fill the gap created by the photoexcitation. This mechanism implies the preservation of the total spin of the system and good overlap between the orbitals of the chromophore and the activator. Due to the strong screening of the 4f orbitals, the Dexter mechanism is unlikely in systems based on lanthanide ions [48].

The second, more widely represented mechanism is proposed by Förster [57] and is known as resonance energy transfer or the dipole-dipole mechanism. In its presence, the ligand again absorbs a photon and transitions to an excited singlet state, after which it undergoes intersystem crossing to enter a triplet state. The dipole moment associated with the relaxation of the excited state of the ligand interacts with the dipole moment of the 4f orbitals of the lanthanide ion, and energy is transferred from the donor to the acceptor. Figure 14 schematically shows how the two processes of energy transfer occur [48].

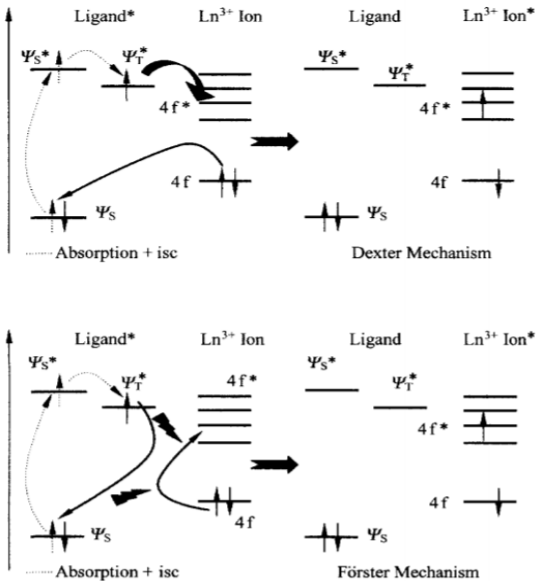

Fig. 14. Dexter exchange mechanism (upper) and Forster resonant energy transfer (down) [48].

3.3.5 Luminescent spectroscopy.

Luminescent spectroscopy is a method for studying the emission of materials under different excitations. From a theoretical perspective, it is a method that allows for the examination of electronic levels that are difficult to observe in absorption mode (forbidden transitions or at low concentrations of the activator), the efficiency of energy transfer between ligands and the activator ion (excitation spectra), the mechanism of energy transfer, and quantum yield – the ratio of radiative to non-radiative relaxation of substances. The latter will be discussed in more detail in the following section.

Luminescent spectra are recorded by irradiating the sample with radiation of a fixed wavelength, and the emitted light from the sample is analyzed using a monochromator. For rare earth elements, their absorption and emission spectra are very weakly influenced by the environment due to screening from their outer electrons. In their case, electronic transitions are generally difficult to observe in absorption mode. Due to negligible Stokes shifts in the spectra of rare earth ions, luminescent spectra can be used to determine the energy of the corresponding electronic levels.

Based on the selection rules, algorithms have been developed to determine the environment around the ion [58–60]. In the luminescent spectra of lanthanide ions, the relative intensities between transitions, the shift in peak positions, and the number of Stark multiplets and their components, which are 2J+1 in number, are most commonly monitored.

Excitation spectra are recorded by monitoring the emission intensity of one of the peaks in the emission spectrum (usually the most intense peak) while varying the excitation radiation. These spectra are typically presented by showing the emission intensity as a function of the excitation radiation. The excitation spectra generally follow the absorption spectrum (ε), modulated by the efficiency of energy transfer (η):

$$Ex=\varepsilon*\eta \quad (34)$$

In the excitation spectrum of materials containing rare earth elements, broad bands are observed, associated with the absorption of the ligand or matrix, indicating energy transfer. Sometimes, much lower intensity bands are also observed, corresponding to the direct absorption of light by the rare earth ion. Usually, the excitation spectra have a similar shape to those of absorption, but with altered intensities. If there is a missing band in the excitation spectrum, it is most likely that this "excitation channel" does not lead to the excitation of the activator ion [58,59].

3.3.6 Quantum yield.

An excited electronic state can relax to the ground state through a number of processes, namely, radiative (fluorescence and phosphorescence) and non-radiative (vibrational and rotational transitions). Also, luminescence can be "quenched" by various chemical substances or the electronic energy can be transferred to a non-emitting state. The relative intensities of these processes are strongly influenced by the nature of the activator and its surrounding environment. Therefore, measuring the quantum yield is a valuable approach in studying the photophysical properties of chromophores and the effect of their surrounding environment [61,62]. Quantum yield (QY) is defined as the ratio of the number of emitted photons Nem to the number of absorbed photons Nabs:

$$QY = \frac{N_{em}}{N_{abs}} \quad (35)$$

There are two experimental approaches for measuring quantum yield, which can be simply divided into a comparative method and an absolute method. In the first method, the quantum yield of the sample under investigation is obtained by comparing its emission spectrum with that of a known standard. This method is very convenient for studying weakly absorbing isotropic systems, such as dilute solutions, but it has serious drawbacks. The chosen luminescent standard must have similar optical properties (absorption and emission) to the material being studied. The comparative method proves unsuitable for anisotropic samples, where the orientation and position of the sample could affect the measurement.

Quantum yield is experimentally determined using an integrating sphere, which can collect all the emitted light from the sample. This attachment also allows for the measurement of absolute quantum yield. In this method, the intensity of the sample's emission is compared with the reduction in the intensity of the excitation radiation both with and without the sample in the sphere.

3.4 Physical method to characterize porous materials.

3.4.1 Low temperature isotherms of adsorption0desorption of gas.

Adsorption is a spontaneous process in which molecules of the adsorbate (liquid or gas) accumulate and concentrate on a solid surface (adsorbent). The forces of attraction between the two are due to electric dipoles, induced dipoles, and quadrupole electrostatic interactions, commonly known as Van der Waals forces. Surface adsorption is possible because the surface energy of the adsorbent is higher, and adsorption lowers the energy of the system. In almost all cases, adsorption occurs as an exothermic process, releasing heat in the range of 10 – 40 kJ/mol, which is comparable to the heat of liquefaction of most gases. This can be explained thermodynamically through Gibbs free energy, for a spontaneously occurring process $\Delta G<0$. During adsorption, the adsorbate molecule loses at least one translational degree of freedom. She can only move along the surface of the adsorbent. The energy of adsorption can be expressed through the Lennard-Jones potential, which accounts for short-range repulsive forces and long-range attractive forces between the adsorbate and the adsorbent. The minimum in the potential curve corresponds to the heat of adsorption [68].

If we consider the following system: a solid body suspended on a spring and placed in a closed environment filled with gas at a certain pressure and volume, the solid body begins to adsorb gas, thereby increasing its mass m, while the pressure in the vessel decreases. In time, equilibrium will be established, and the amount of adsorbed gas can be determined by the decrease in pressure in the vessel or by the increased mass of the sample. The amount of adsorbed gas can be expressed as a function of pressure, temperature, the mass of the adsorbent, as well as the nature of the adsorbent and the adsorbed gas [69]. The results of adsorption experiments can be grouped into one of the five isotherms classified by Brunauer, Deming, Deming, and Teller [70], as well as the special stepwise isotherm. Figure 17 shows the six standard isotherms. Isotherm type I is associated with microporous materials, type III and V with the adsorption of water molecules, while type II relates to adsorption on non-porous bodies. Of practical and scientific significance is the type IV isotherm, which is associated with adsorption in mesoporous materials. Isotherms type IV and V exhibit hysteresis. The lower part of the curve describes the adsorption of gas, while the upper part describes desorption [69]. The stepwise isotherm (type VI) is observed when adsorption occurs on a homogeneous surface [71]. It is most commonly observed on smooth materials like graphene, where individual layers are adsorbed in a stepwise manner.

Isotherm type I is distinguished from the others by its well-defined plateau and the absence of adsorption when the gas pressure in the system increases. The pores in nanoporous materials have a diameter of less than 5 nm and do not have a sufficiently large volume to form many layers. It is assumed that upon reaching the plateau, the adsorption monolayer is completely filled and no more molecules can be adsorbed. Besides various coals, such isotherms are also exhibited by some xerogels made from silicon, titanium, aluminum, and tin oxides. The second type of isotherm is observed in non-porous samples. In their case, gas molecules can only be adsorbed on the surface, not within the volume of the materials. They lack hysteresis and saturation of the samples because adsorption layers can freely form or evaporate. Type III isotherm is associated with the adsorption

of water on non-porous materials. In her analysis, the geometric models are very similar to those of isotherm type II. Type V isotherm is observed in the adsorption of water in nanoporous and mesoporous materials. The saturation plateau is due to the filling of the pores, while hysteresis is a consequence of Kelvin's law of capillary condensation.

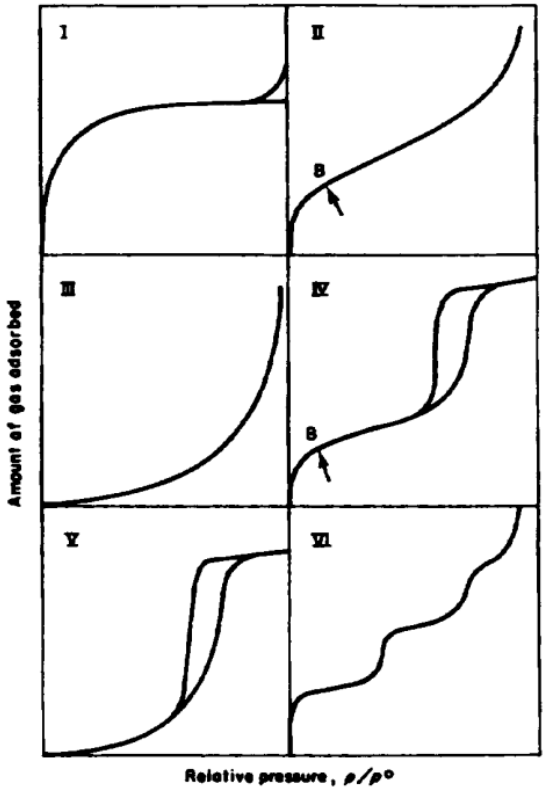

Fig. 17. Types of isotherms according to Brunaur, Deming, Deming and Teller nomerclature [72].

Mesoporous materials, such as oxide aerogels and xerogels, exhibit a type IV isotherm. This type of isotherm is distinguished by its characteristic hysteresis. The amount of adsorbed gas at the same relative pressure p/p0 is always higher in the desorption branch than in the adsorption branch. This is possible thanks to what is known as capillary condensation. This effect was first described by Zsigmondy, relying on Lord Kelvin's law. The Kelvin law states that the equilibrium vapor pressure p above a concave meniscus is always lower than the vapor pressure of the liquid at a given temperature.

$$ln\frac{p}{p_0} = \frac{-2\sigma V_l}{RT}\frac{1}{r_m} \tag{38}$$

Here, p/p0 is the relative equilibrium vapor pressure above a concave meniscus with a radius of curvature rm, while σ and Vl are the surface tension and molar volume of the liquid phase. R and T denote the universal gas constant and absolute temperature. According to Szigmondy, the surface of the adsorbent is filled with a monolayer of adsorbed molecules until the pressure

becomes sufficient to initiate capillary condensation, first in the smallest pores of the material. Capillary condensation begins at the relative pressure at which hysteresis closes. As the pressure increases, larger pores fill up until saturation is reached. The Kelvin equation allows for the calculation of the pore size of the material, as the pressure at which condensation will occur in a given pore p directly depends on the size of the pore rm. The process of capillary condensation begins after a monolayer has been filled on the surface of the pore; the resulting measurement for the pore radius does not take into account the thickness of this monolayer [69].

3.5 Literature review – composite and luminescent materials.

This section discusses research in the field of aerogels, luminescent materials, and hybrid composite materials. Various methods for obtaining, characterizing, and tuning the properties of materials are fundamental to materials science. The structure-property relationship is an important analytical method in chemistry when it comes to solid-phase systems.

In addition to classical applications in thermal and sound insulation, aerogels are finding increasingly wide use in other areas. Optical materials for sensing, biomedical applications, sorption of organic pollutants and spilled oil in water, catalyst supports – nanoreactors in the pores of gels, protective matrices for luminescent components, and many more.

The low thermal conductivity (<0.03 W/m.K) makes aerogels one of the most attractive insulating materials in space technologies. The Mars rover of the PATHFINDER mission used aerogels to insulate its instruments. Despite the enormous daily temperature fluctuations of over 60 K, a constant stable temperature of 21 °C is maintained in its interior. The European Space Agency is applying similar technologies for its satellites. Thermal insulation is not the only application of aerogels in space technologies. The Stardust program successfully utilizes them for collecting cosmic dust and particles. Aerogels are used to protect space mirrors and fuel tanks.

4. Experiments.

4.1. Obtaining and characterization of aerogel granules and powders.

4.1.1 Obtaining of SiO_2 granules with different degree of hydrophobicity.

The silica gel granules were obtained using a two-step sol-gel technology, as described in [20]. The methodology is a modified version of that developed by N. Danchova and co-authors [25], with the main difference being that all steps are carried out at room temperature. The following reagents were used: tetraethoxysilane (TEOS) (Sigma, St. Louis, MO, USA), absolute ethanol (abs EtOH 99.6%) (Sigma), distilled water (dH2O), trimethylchlorosilane (TMCS) (Sigma); acetone, n-hexane, hydrochloric acid, and ammonia solution were supplied by local vendors. All reagents used are of analytical grade purity and have been used without further purification.

The scheme for obtaining aerogel granules with varying degrees of hydrophobization is shown in Fig. 28. The first step is the hydrolysis of tetraethoxysilane in an acidic environment. In a polypropylene jar with a lid, 10 mL of TEOS and 7.8 mL of absolute ethanol have been mixed. The solution is stirred for 5 minutes with an electromagnetic stirrer, after which 0.805 ml of dH2O and an acid catalyst for the hydrolysis process – 0.140 mL of 0.23M HCl – are added. Under these conditions, the molar ratio of TEOS to water is nTEOS:nH2O=1.17. The hydrolysis is carried out for about 1 hour under constant stirring. The second step is the addition of 6 ml of the alkaline catalyst (cat G), which is a solution of ammonia in water and ethanol with a pH of 11. In a neutral and slightly alkaline environment, the reaction of polycondensation is promoted, leading to the formation of siloxane bridges and the production of oligomers, their crosslinking, and bonding. The gel will set in 10 minutes. The fresh gels are covered with 20 mL of absolute ethanol, and solvent exchange occurs in the pores while the gel matures for 24 hours. In this way, some of the unreacted molecules and the salts formed in the pores of the gel are removed. The reaction of polycondensation continues, and the gel becomes more cross-linked, which improves its mechanical properties.

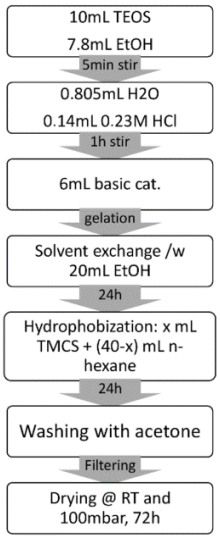

Fig. 28. Obtaining of SiO_2 granules with different degree of hydrophobicity

In order to obtain hydrophobic powders and granules, the surface of the gel must be chemically modified. For this purpose, a hydrophobizing mixture consisting of TMCS and n-hexane is prepared. Five gels have been obtained, which are hydrophobized with different hydrophobizing mixtures. The total volume is fixed at 40 mL, while the volume (x) of TMCS in the mixture varies. Thus, 5 mixtures are prepared with a composition of x = 0, 2, 4, 6, 8 mL TMCS and 40-x mL n-hexane. After the gel has matured, the ethanol is decanted, and the gel is crushed into granules and covered with the hydrophobizing mixture. In this way, the samples named MJ0 – covered with 40mL of n-hexane, MJ2 – 2mL of TMCS and 38mL of n-hexane, MJ4 – 4mL of TMCS and 36mL of n-hexane, MJ6 – 6mL of TMCS and 34mL of n-hexane, and MJ8 – 8mL of TMCS and 32mL of n-hexane were obtained. Trimethylchlorosilane reacts violently with remaining hydroxyl groups on the surface of silica gel, releasing hydrogen chloride gas, while the polar hydrophilic –OH groups are replaced with nonpolar -Si(CH3)3 groups. The gels are kept for 24 hours in the hydrophobizing mixture, after which they are filtered and thoroughly washed with acetone. The samples were dried using a subcritical method – at room temperature and under vacuum. A vacuum furnace has been used, equipped with a diaphragm pump with a flow rate of 30 L/min. The volume of the furnace is 15 L. The samples were held for 72 hours at a pressure of 100 mbar.

For these reasons, contact angles of water droplets with the obtained granules and powders have not been measured. For the purposes of this work, the hydrophobicity degree α of the samples MJ0-MJ8 is defined as the molar ratio of the hydrophobizing agent TMCS to the precursor TEOS.

$$\alpha = n_{TMCS}/n_{TEOS} \quad (44)$$

The studied properties of the samples are summarized as a function of the thus defined degree of hydrophobicity. Table 4 provides the designations of the samples, their degree of hydrophobicity, and their apparent density. (bulk density).

Sample	α	ρ, g/mL
MJ0	0	0,45
MJ2	0,352	0,33
MJ4	0,7	0,23
MJ6	1,055	0,18
MY8	1,407	0,2

Table 4. Samples with different degree of hydrophobicity and their apparent dencities.

It is observed that with an increase in the degree of hydrophobicity, the density of the samples decreases, with saturation occurring at α=1.055. (MJ6). This is a well-known phenomenon [73], which is due to the densification of the granules during drying. During subcritical drying, the capillary pressure in the pores leads to their destruction and the shrinkage of the samples. By modifying the surface, the wetting angle of the gel walls from the solvent can be altered, which in turn can reduce the capillary pressure, following Young's equation. From the densities, it can be observed that the degree of hydrophobization has an impact on the physical properties of the gels. The hydrophilic gel MJ0 has a density of 0.45 g/mL, which is more than twice that of the hydrophobic gels MJ6 and MJ8 – 0.18 and 0.2 g/mL, respectively.

X-ray structural analysis shows that the obtained samples are amorphous. A broad amorphous halo is observed, and the well-defined diffraction peaks characteristic of crystalline phases are absent (Fig. 30). The following sections examine how the degree of hydrophobicity affects the structure and morphology of the samples.

Through IR spectroscopy, it is possible to determine what structural elements are present, as well as their arrangement (siloxane rings and chains, the valence angles between the tetrahedra). From low-temperature isotherms, additional information can be extracted about the size of the pores, their shape, microstructure, and morphology.

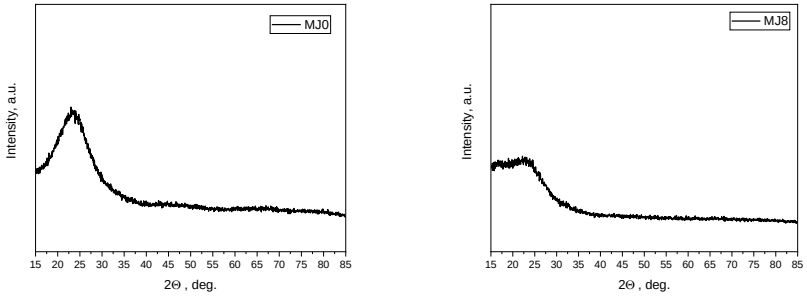

Fig. 30. XRD diffraction pattern of hydrophilic gel MJ0 and hydrophobic MJ8.

4.1.2 IR spectroscopy – structure and hydrophobicity.

All FTIR spectra were recorded on a Bruker ALPHA II Platinum (Billerica, MA, USA)—an ATR spectrophotometer equipped with a diamond attachment. The resolution of the spectra is

1 cm-1, and 64 scans were made for the sample. For easier comparison of the spectra, they have been normalized to the most intense peak at 1080 cm-1. The spectra of the obtained silica gel granules were mathematically treated with nonlinear fitting using the least squares method with 5 or 6 Gaussian curves in the region of 900-1300 cm-1. In glasses and other amorphous materials, the forces of the bonds (the force constants) of the same chemical bonds differ due to inhomogeneities and other local effects. For this reason, the vibrations from the same chemical groups can be described as a Gaussian distribution of frequencies from Lorentzian oscillators.

The non-homogeneous broadening of the peaks leads to a Gaussian shape of the stripes [34], as discussed in the previous sections. In this way, the positions and relative intensities corresponding to the antisymmetric vibration □as(Si-C-H) at 1260 cm-1, the transverse and longitudinal vibrations of the four- and six-membered siloxane rings that make up the matrix, and the antisymmetric □as(Si-OH) at 950 cm-1 were found. The spectra of samples MJ0, MJ2, MJ4, MJ6, and MJ8 are shown in Fig. 31. Dense, amorphous silicon dioxide has been used as a standard.

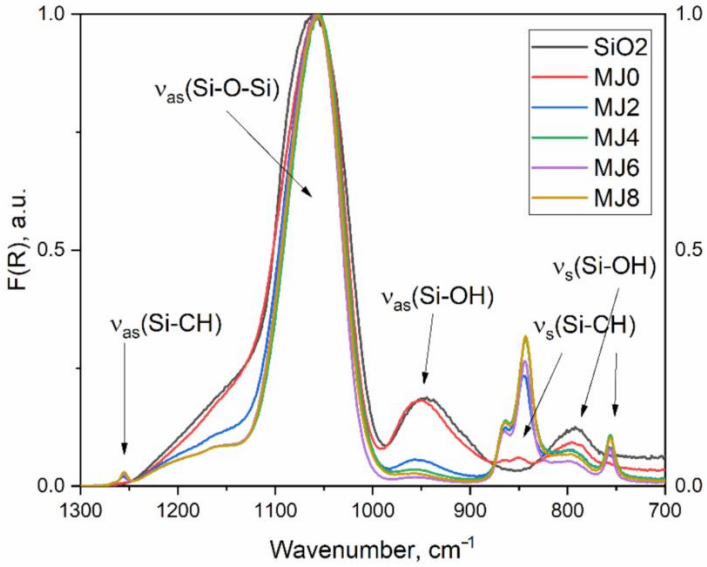

Fig. 31. ATR-IR spectra of samples MJ0, MJ2, MJ4, MJ6 and MJ8 and amorphous silica oxide.

The main analysis was conducted on the region called the "fingerprint" from 700-1300 cm-1. Outside of it, there can be found a few peaks. The most intense one is a broad band around 3000-3600 cm-1. Peaks can also be observed at 1630 and 1274 cm-1, which correspond to the vibrations of the water molecule and ethanol, respectively. They can be observed if the sample is not sufficiently dried. The region can be used to analyze the structure of silicate materials. We can further divide this region into two, namely the one from 1300–900 cm−1, where the antisymmetric νas(Si-O-Si) and νas(Si-O-H) are located, and the one from 700 to 900 cm−1, where peaks corresponding to the symmetric vibrations νs(Si-O-Si) and νs are found.(Si-CH3). The broad band in the range of 1000-1200 cm-1 consists of four overlapping bands, which correspond to the transverse (TO4 and TO6) and longitudinal vibrations (LO4 and LO6) of four- and six-membered siloxane rings in the structure of the gels - (SiO)4 and (SiO)6 (shown in Figure 10). [38,74,75]. The separation of transverse and longitudinal components is due to distant Coulomb interactions.

An important peak observed in this area is the low-intensity peak at 1260 cm-1, which is attributed to the antisymmetric □as.(Si-C-H). This peak is observed only in the hydrophobized samples: MJ2, MJ4, MJ6, and MJ8, and is due to the replacement of hydroxyl groups with hydrophobic –Si(CH3)3 groups. In the pure sample of SiO2, this peak at 1260 cm-1 is also not observed. This weak but important peak indicates the hydrophobization of the sample without providing information about the change in the structure of the silicate network during hydrophobization

Another peak, whose intensity strongly depends on the composition, is the one at 950 cm-1. It responds to the vibrations of Si-OH groups. It is noted that its intensity significantly decreases during the hydrophobization of the sample. Even with the MJ8 sample, which has a hydrophobicity coefficient of α=1.405, its intensity is not zero. This shows that not all hydroxyl groups are substituted during hydrophobization. The hydrophobic –Si(CH3)3 groups are too bulky to replace all available hydroxyl groups. For steric reasons, if there are too many close hydroxyl groups, not all of them will be able to be substituted. The intensity of the band at 800 cm-1 also decreases with the increase in the hydrophobicity of the samples. It is due to the symmetrical vibrations of Si-OH groups. In contrast, intense bands appear at 760 and 860 cm-1, which are due to symmetric vibrations of Si-C-H groups. The spectrum of the hydrophilic sample MJ0 overlaps very well with that of amorphous silicon dioxide. All samples have a broad and intense band in the region of 1000-1200 cm-1, with a maximum at 1080 cm-1.

In order to extract more information from the spectra, a nonlinear deconvolution of the region 900-1300 cm-1 has been performed. For the MJ0 sample, five Gaussian functions were used to describe the peak centered at 950 cm-1, corresponding to the vibrations of hydroxyl groups, and four functions for the broad band in the range of 1000-1200 cm-1, where the transverse and longitudinal vibrations of four- and six-membered siloxane rings (TO4 and TO6, LO4 and LO6) are located. For the remaining samples, MJ2, MJ4, MJ6, and MJ8, six functions were used to describe the same peaks, including the one at 1260 cm-1, which is due to hydrophobization. Figure 32 shows the results after the deconvolution of the spectra of the hydrophilic sample MJ0 and the hydrophobic sample MJ4. Mathematically, this approach leads to a very high correlation coefficient R2 between 0.99 and 0.999, which is an indicator of its reliability. The number of strips follows the logic of the "Central Forces Model," and the only fixed parameter of the fit is y0=0; y = y0 + A/(w*sqrt(pi/(4*ln(2)))) * exp(-4*ln(2)*(x-xc)^2/w^2).

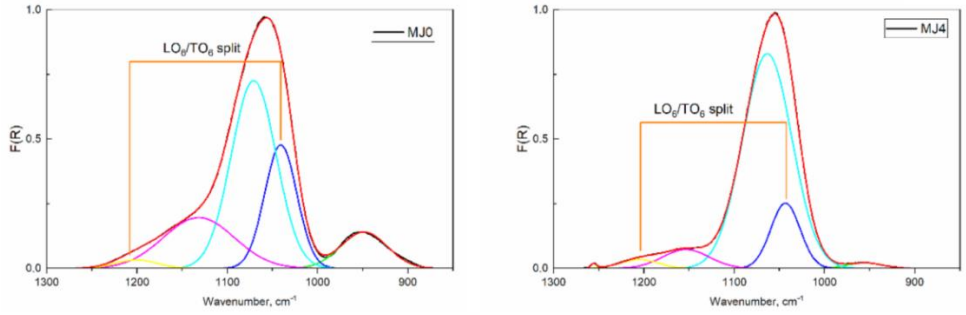

Fig. 32. Nonlinear deconvolution with five Gaussian curves for the hydrophilic sample MJ0 and six Gaussian curves for the hydrophobic sample MJ4. The red curve is the total spectral curve, and its area is the sum of the areas of the component curves..

The figure shows the splits of transverse and longitudinal vibrations. For the six-membered siloxane rings, the longitudinal vibrations (LO6) occur at 1220 cm-1, while the transverse vibrations (TO6) occur at 1050 cm-1. The splitting in four-membered rings is less, and their longitudinal vibrations (LO4) occur at 1150 cm-1, while the transverse vibrations (TO4) occur at 1080 cm-1. The splitting (LO6-TO6) in six-membered rings is 160 cm-1, while in four-membered rings (LO4-TO4) it is 80 cm-1. Six-membered rings are less strained with an average angle between adjacent tetrahedra (SiO4^2-) of about 140 degrees, while in smaller rings it is around 120 degrees. As a result, four-membered rings are more strained and thermodynamically unfavorable, but they form more quickly during the hydrolysis and polycondensation of TEOS. In the following table 5, the data from the nonlinear deconvolution of the spectrum in the region of 900-1300 cm-1 is summarized.

For each sample, the splitting LO6-TO6 is provided, along with the origin of the corresponding peak, its integral area, the full width at half maximum (FWHM), intensity (height), center (position of the maximum), and relative intensity (area as a percentage of the total area of the peaks). The LO-TO splitting for six-membered rings is closer to that of α-quartz at 160 cm-1 than to that of amorphous silicon dioxide at 140 cm-1.

Sample; TO6/LO6 splitting	Peak index	Peak origin	Integrated area	FWHM	Intensity	Center	Area
				cm−1	-	cm−1	%
MJ0	1	ν_{as}(Si-OH)	9,10	60.82	0.14	948.81	9,40
160.3 cm^{-1}	2	TO6	21.36	42.05	0.48	1040.84	22,06
	3	TO4	45.10	58.38	0.73	1070.83	46.58
	4	LO4	19.37	92.53	0.20	1131.65	20.01
	5	LO6	1,90	54.55	0.03	1201.10	1,96
	6	ν_{as}(Si-C-H)	0.00	0.00	0.00	0.00	0.00
MJ2	1	ν_{as}(Si-OH)	2,10	55.53	0.04	956.01	2.64
163.8 cm^{-1}	2	TO6	31,03	44.99	0.65	1045.12	38.58
	3	TO4	35.47	52.48	0.63	1075.94	44.10
	4	LO4	10,79	94.36	0.11	1143.47	13.42
	5	LO6	0.95	42.67	0.02	1208.96	1.18
	6	ν_{as}(Si-C-H)	0.09	6,84	0.01	1256.28	0.11
MJ4	1	ν_{as}(Si-OH)	1,06	45.96	0.02	955.75	1.42
161.8 cm^{-1}	2	TO6	10,25	38.17	0.25	1043.31	13.71
	3	TO4	56.78	64.25	0.83	1063.39	75.93
	4	LO4	4,72	60.74	0.07	1153.59	6.31
	5	LO6	1,81	49.63	0.03	1205.14	2.42

	6	ν_{as}(Si-C-H)	0.16	7,89	0.02	1255.53	0.21
MJ6	1	ν_{as}(Si-OH)	0.53	46.40	0.01	957.00	0.72
165.7 cm^{-1}	2	TO6	14.51	38.01	0.36	1045.07	19.82
	3	TO4	50.91	59.74	0.80	1068.75	69.53
	4	LO4	5,86	72.22	0.08	1155.84	8.00
	5	LO6	1,27	44.57	0.03	1210.80	1.73
	6	ν_{as}(Si-C-H)	0.15	7,57	0.02	1255.78	0.20
MJ8	1	ν_{as}(Si-OH)	0.85	48.67	0.02	958.34	1.13
159.1 cm^{-1}	2	TO6	9,93	37.15	0.25	1044.92	13.30
	3	TO4	57.41	64.44	0.84	1065.19	76.92
	4	LO4	4,24	55.74	0.07	1154.85	5.68
	5	LO6	45384,00	50.21	0.04	1204.04	2.73
	6	ν_{as}(Si-C-H)	0.18	7,89	0.02	1255.29	0.24

Table 5. General data from the nonlinear Gaussian deconvolution of IR spectra in the region of 900-1300 cm-1. The name of the sample shows the parameter TO6-LO6 of the splitting.

Longitudinal vibrations (LO) are more sensitive to the environment than transverse ones. (TO). This can be demonstrated by the change in the positions of the peaks. The positions of the longitudinal vibrations vary by about 10 cm-1 for LO6 and 20 cm-1 for LO4. While TO4 and TO6 vary by 5 and 10 cm-1, respectively. As the degree of hydrophobicity of the samples increases, the intensity of the shoulder decreases towards higher energies. The intensity of the LO6 vibration decreases drastically, while that of the TO4 increases. The total area of the peaks of six-membered siloxane rings decreases with increasing hydrophobicity of the samples from 23.26 to 11.97, while that of the four-membered rings remains almost unchanged. This is very clearly seen in Fig. 33, where the relative intensities of the peaks in the range of 900-1300 cm-1 are presented.

4.1.3 BET isotherms – morphology.

The textural properties of the obtained samples with different hydrophobicity MJ0, MJ2, MJ4, MJ6, and MJ8 were analyzed using low-temperature nitrogen adsorption-desorption isotherms. The isotherms were recorded on a Quantachrome Instruments NOVA 1200e apparatus (Boynton Beach, FL, USA) at 77.4 K. The obtained isotherms were processed using the Brunauer–Emmett–Teller (BET) equation to obtain information about the specific surface area SBET of the samples. The specific volume Vt of the pores and their average diameter Dav have been determined at relative pressures p/p0 close to 0.99. The pore size distribution was constructed using nonlocal density functional theory (NLDFT), employing equilibrium models of cylindrical pores. The fractal multilayer isotherm of Frenkel–Halsey–Hill has been used to determine the surface fractal coefficient of the samples [76–78]. The calculations were made using the device's built-in

software. From the analysis of the hysteresis loop shape, a conclusion has been drawn regarding the shape and geometry of the pores in the gels [79]. Before taking the isotherms, all samples were degassed at 150 °C for 16 hours.

The obtained low-temperature isotherms of samples MJ0, MJ2, MJ4, MJ6, and MJ8 are shown in Figure 34. All samples have an isotherm of type IV, which according to the UIPAC classification is associated with mesoporous materials (pore diameter distribution between 2 and 50 nm) [42]. The hydrophilic sample MJ0 and the weakly hydrophobic sample MJ2 have a low hysteresis closing point. For this reason, the hysteresis cycle is classified as type H2. This type is common in amorphous glasses and gels. Geometric models connect H2-type hysteresis with ink bottle-type pores, meaning a closed pore with a narrow neck and a much wider body. Capillary condensation begins in smaller pores at pressures lower than the equilibrium pressure for the corresponding temperature. Therefore, during the desorption process, the condensed nitrogen is first evaporated from the larger pores. When the flask has the shape of a bottle, the liquid inside evaporates only when a sufficiently low pressure is reached, at which point the liquid evaporates through the narrow "neck" of the flask, after which the entire contents of the flask escape.

Therefore, in the desorption curve, there is no noticeable mass loss of the sample until a sufficiently low critical relative pressure is reached, at which point there is a sharp release of gas and an almost stepwise decrease in the mass of the sample being analyzed [72,80]. It is already known that these geometric models provide an overly simplified picture, but they give a good idea of the geometry of the studied materials.

The hydrophobic samples MJ4, MJ6, and MJ8, for their part, exhibit H3-type hysteresis. There is no saturation of the samples observed above a certain relative pressure of nitrogen. This type of hysteresis cycle is observed when the pores are cracks between plate-like particles. This geometry allows particles to move relative to each other and to separate. This allows the samples to adsorb more nitrogen than the actual volume of the pores under normal conditions [20,72,81–83]. From this, it can be concluded that the hydrophobicity of the samples and the molar ratio of TMCS/TEOS have a strong influence on the final geometry and morphology of the pores.

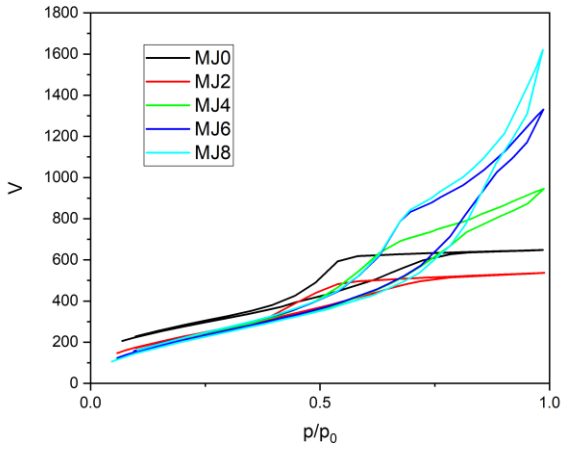

Fig. 34. Low-temperature isotherms of adsorption-desorption of nitrogen at 77 K on samples with varying degrees of hydrophobization MJ0, MJ2, MJ4, MJ6 и MJ8.

Table 6 summarizes the data for SBET, Vt, and Dav in relation to the degree of hydrophobization α of the samples MJ0, MJ2, MJ4, MJ6, and MJ8, obtained from the analysis of low-temperature BET isotherms. A decrease in the specific surface area SBET of the samples is observed with an increase in the degree of hydrophobicity. The specific surface area decreases very rapidly from 1008 m²/g for the hydrophilic sample MJ0 to 860-890 m²/g for the other samples. Overall, the specific volume Vt and the average diameter Dav of the pores increase with the increase in hydrophobicity of the samples. The specific volume of the samples can increase by more than two times during hydrophobization. In the hydrophilic test MJ0, it is 1.1 cm3/g, while in the hydrophobic MJ8 it is 2.5 cm3/g. The average diameter of the pores follows a similar relationship. It increases monotonically from 4 nm for the MJ0 sample to 7 nm for the hydrophobic samples MJ6 and MJ8. Hydrophobization of the pores leads to lower interfacial tensions in the pores during drying. Lower tensions during drying do not damage the pores as much, and the final material has a lower density. The specific volume of the pores in the samples is in good agreement with the measured bulk densities of the obtained granules. The hydrophobic samples have a larger average pore diameter and a pore distribution skewed towards larger diameters (Fig. 35). Smaller pores (sample MJ0) are associated with a better-developed surface SBET. In the hydrophobic samples MJ6 and MJ8, the smallest pores may be filled with bulky groups –Si(CH3)3. For comparison, the measured data for the commercial product hydrophobic aerogel granules from CABOT ™ is provided. They are obtained through the supercritical method, but have a lower specific surface area of <700 m²/g, which is about 20% lower than that of the hydrophobic gels MJ4, MJ6, and MJ8. In contrast, its density is 35% lower than that of the lightest hydrophobic gel in the series – MJ8. The average diameter of the pores is much larger than those of the MJ series.

Sample	α	S_{BET}, m^2/g	V_t, cm^3/g	D_{av}, nm
MJ0	0	1008	1,1	4.0
MJ2	0.352	888	0.83	4,6
MJ4	0.7	860	1,47	6.0
MJ6	1.055	872	2,06	7.0
MY8	1.407	862	2,51	7.0
CABOT	NA	699	3.8	21

Table 6. General data for SBET, Vt, and Dav regarding the degree of hydrophobization α of the samples MJ0-, MJ2, MJ4, MJ6, and MJ8, calculated from the low-temperature adsorption-desorption isotherms of nitrogen at 77K.

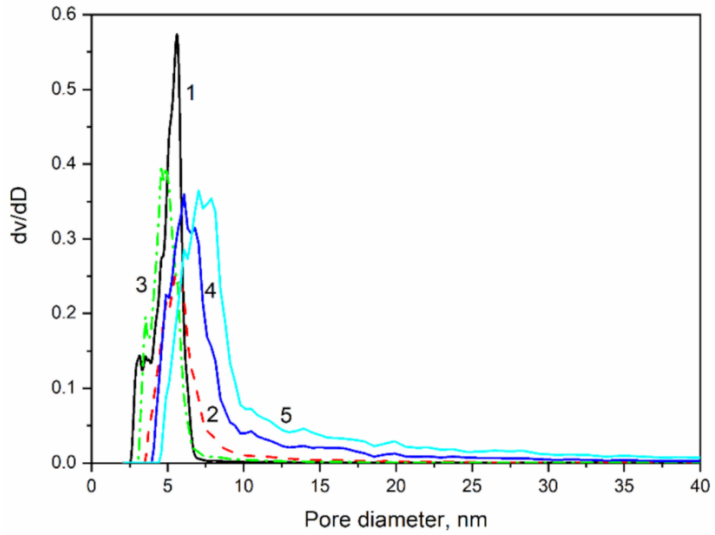

Fig. 35. Pore diameter distribution for samples: 1-MJ0, 2-MJ2, 3-MJ4, 4-MJ6 и 5- MJ8.

The probes MJ0, MJ2, and MJ4 have narrower distributions of pore diameters. When testing MJ6 and MJ8, the distribution is wider and there is a shoulder towards the larger diameters. It is also observed that they practically have no pores with diameters smaller than 4 nm.

4.2 Obtaining, photophysical properties and structure of luminescent composite materials based on SiO_2:$[Eu(phen)_2](NO_3)_3$ и SiO_2:$[Tb(phen)_2](NO_3)_3$.

4.2.1 Obtaining.

In a series of publications, the successful synthesis of functionalized aerogel granules and powders with luminescent hybrid complex compounds of europium (III) and terbium (III) has been investigated, comparing the properties of the pure materials and the obtained composite materials [21,84,85].

This chapter provides a detailed description of the influence of the matrix on the photophysical properties of the final composite materials containing the complexes [Eu(phen)2](NO3)3 and [Tb(phen)2](NO3)3, a topic that has not been addressed in any previous publications on the subject. The set goal has a practical orientation due to the presence of a wide variety of silicate porous materials with different degrees of hydrophobicity: fumed silica, CABOT LUMIRA granules, low cristobalite, and others.

Different matrices were used, such as the aerogel granules and powders MJ0, MJ2, MJ4, MJ6, and MJ8, which have varying degrees of hydrophobicity, as described in the previous chapter, leading to different morphologies, traces of water, and other solvents. These complex compounds of the rare earth elements europium and terbium have been selected due to their easy synthesis and incorporation into matrices, as well as their application as green and blue components in sensor materials and as light sources. Due to their low solubility in water and

ethanol, these complexes can be synthesized by precipitation from solutions. When mixing ethanol solutions of the corresponding ion and a solution of 1,10-phenanthroline, a microcrystalline precipitate of the corresponding complex is formed.

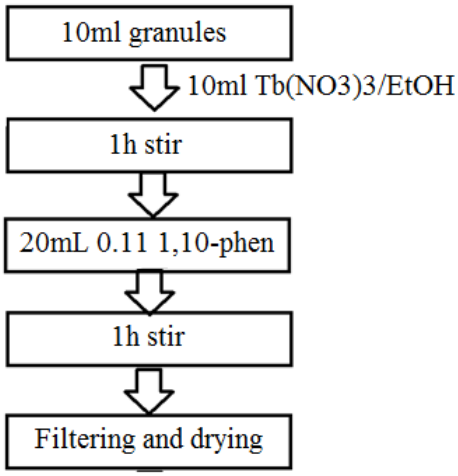

Fig. 38. Scheme for production of aerogel based luminescent composite materials containing $[Eu(phen)_2](NO_3)_3$ and $[Tb(phen)_2](NO_3)_3$ [86].

Thus, samples containing 0.35% [Eu(phen)2](NO3)3 were obtained in matrices MJ0, MJ2, MJ4, MJ6, and MJ8, named respectively MJ0_Eu, MJ2_Eu, MJ4_Eu, MJ6_Eu, and MJ8_Eu. Similarly, the composite materials with 0.35% terbium complex are named: MJ0_Tb, MJ2_Tb, MJ4_Tb, MJ6_Tb, and MJ8_Tb. The names of the obtained materials, the matrix used, their chemical composition, and degree of hydrophobicity are summarized in Table 8. Photos of the obtained luminescent samples are shown below in Fig. 39. For the sake of completeness in the measurements, a hydrophilic matrix MJ0 was prepared, doped only with 1,10-phenanthroline, and a hydrophobic matrix MJ8, also doped solely with phenanthroline. The obtained samples are named, respectively, MJ0_phen and MJ8_phen. The structural studies were conducted on a hydrophobic matrix MJ4 doped with 1% [Eu(phen)2](NO3)3 – sample MJ4_.01Eu and doped with 1% [Tb(phen)2](NO3)3, named MJ4_0.01Tb.

The properties of the obtained composite materials have been compared with the properties of the pure luminescent complexes [Eu(phen)2](NO3)3 and [Tb(phen)2](NO3)3, which are referred to, for simplicity, as Euphen and Tbphen, respectively [86].

Sample	Chemical composition	α
Euphen	$[Eu(phen)_2](NO_3)_3$	–
MJ0_Eu	SiO_2:0.0035Euphen	0
MJ2_Eu	SiO_2:0.0035Euphen	0.352
MJ4_Eu	SiO_2:0.0035Euphen	0.7
MJ6_Eu	SiO_2:0.0035Euphen	1.055
MJ8_Eu	SiO_2:0.0035Euphen	1.407
Tbphen	$[Tb(phen)_2](NO_3)_3$	–

MJ0_Tb	SiO_2:0.0035Tbphen	0
MJ2_Tb	SiO_2:0.0035Tbphen	0.352
MJ4_Tb	SiO_2:0.0035Tbphen	0.7
MJ6_Tb	SiO_2:0.0035Tbphen	1.055
MJ8_Tb	SiO_2:0.0035Tbphen	1.407
MJ0_phen	SiO_2:0.0075phen	0
MJ8_phen	SiO_2:0.028phen	1.407

Table 8. Obtained samples with different matrixes contaiing $[Eu(phen)_2](NO_3)_3$ and $[Tb(phen)_2](NO_3)_3$.

4.2.2 UV-Vis-NIR spectra in diffuse reflectance mode.

Optical spectroscopy in diffuse reflection mode provides information about the absorption properties (maximum, half-width, intensity) of the obtained powdered samples. This is how the absorption peaks can be found, through which the sample can be irradiated to subsequently investigate its luminescence, an algorithm used in the present study.

All spectra in diffuse reflection mode were recorded using an Agilent (Santa Clara, CA, USA) Cary 5000 spectrophotometer with a mounted "Mantis" type attachment. A white standard from Spectralon™ has been used for the range of 200-2500 nm. Ho2O3 was used as a spectroscopic standard for the positions of the peaks and relative intensities [87]. Spectra were taken from samples doped with 1% luminescent complex, MJ_0.01Eu and MJ_0.01Tb. The Kubelka-Munk function F(R) has been calculated from the reflection (%R) spectra of the samples.

The measured spectra are shown in Fig. 40. A spectrum of an undoped silicate aerogel is provided. Due to the low concentrations and weak forces of the f-f transitions oscillators in rare earth ions, they are not observed in the reflective spectra. In all samples, stripes are observed in the near-infrared region, originating from the matrix. Between 2250 and 2400 nm, there are combination vibrations and overtones from the SiO2 matrix. The peaks at 1940 cm-1 and 1950 cm-1 correspond to overtone vibrations of water molecules and clearly indicate that water molecules are retained in the matrix even after hydrophobization. This means that hydrophobization alone is not sufficient to remove all the water without conducting prolonged heating of the samples. Also, in the NIR region of the spectra of the doped samples MJ_0.01Eu and MJ0_0.01Tb, peaks of 1,10-phenanthroline are observed. The peak at 1186 nm and the doublet at 1696 and 1745 nm correspond to C-H vibrations from an aromatic core, but the maxima are slightly shifted compared to pure benzene due to the presence of the heteroatom N in the cycle [33].

Unlike pure SiO2, the doped samples MJ_0.01Eu and MJ_0.01Tb exhibit intense absorption bands in the UV region. Two intense transitions with charge transfer are observed at 220 and 262 nm, which are characteristic of oxide glasses and ceramic materials [60]. These

transitions partially overlap with electronic transitions in S0→Sn>1 in the molecule of 1,10-phenanthroline [88]. The absorption of the silicate matrix (sample GR0) at around 220 nm (LMCTT) is clearly visible in the same figure. Therefore, the high intensity and spectral splitting in the ultraviolet region of the hybrid complexes is due to three transitions: matrix LMCTT, O2-→Si4+ (220 nm); LMCTT O2-→Ln3+ 260 – 280 nm, and S0→Sn>1 in the molecule of 1,10-phenanthroline. The first two transitions are underestimated in the literature, despite their significant intensity used in the lighting industry [88].

The ligand 1,10-phenanthroline has an intense transition around 350 nm, which appears as a shoulder in these spectra. This is his transition from the ground state to the excited singlet state S0→S1 [55,89], which will play a key role in the excitation of the luminescence of the complex. The transitions in the molecule of 1,10-phenanthroline S0→T1 and S0→T2 at 414 and 490 nm are of low intensity.

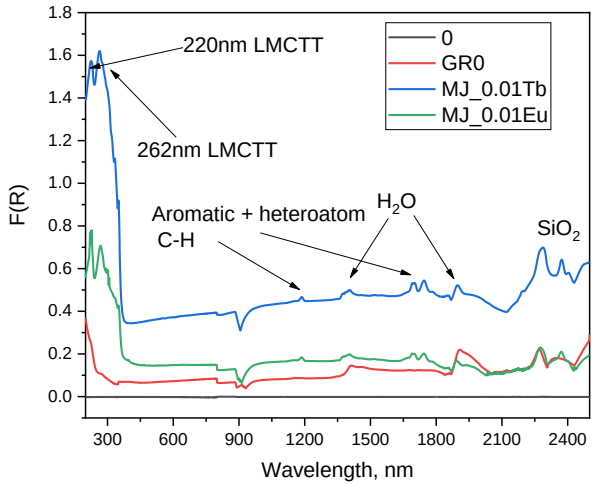

Fig. 40. UV-Vis-NIR spectra in diffuse reflection mode on composite samples doped with luminescent complexes MJ_0.01Eu and MJ_0.01Tb. For comparison, a spectrum of the non-subsidized sample GR0 is provided.

4.2.3 Emission and excitation spectra. Quantum yield.

The optical properties of the obtained samples have been studied using luminescence spectroscopy methods. Spectra of luminescence and excitation have been recorded, and the quantum yields of the luminescent samples have been measured. All spectra and measurements were obtained using the Perkin Elmer FL 8500 fluorimeter. The emission and excitation spectra were obtained using a variable angle solid sample holder attachment (N4201014) with a holder for powdered samples. (N4201032). Spectra are recorded under identical spectroscopic conditions: excitation radiation, scanning speed, and optical slits. For all emission spectra, an excitation wavelength of λ=350 nm was used, which aligns well with the intense absorption band of the

ligand 1,10-phenanthroline. The intensity of the most intense emission line of the samples was monitored against the wavelength of the excitation radiation for the excitation spectra. For the samples doped with Eu (III), this is the band at 615 nm (5D0→7F2), and for those with Tb (III), this is the band at 542 nm (5D4→7F5). The absolute quantum yields were measured in an integrating sphere (N4201017) using the method of Suzuki et al. [90].

The obtained results were compared with those of the pure luminescent complexes [Eu(phen)2](NO3)3 and [Tb(phen)2].(NO3)3. The integral intensities of each peak were calculated after nonlinear Gaussian deconvolution, through which the areas were derived, with a high correlation coefficient R2=0.99 – 0.995, a methodology described in previous chapters.

From the emission spectrum, the color RGB coordinates (x, y, z) of the obtained composite materials have been calculated. A program has been used that follows the algorithm from [91]. The obtained data were compared with those calculated from the online platform, and no differences greater than 1% were found [86].

The emission spectra of samples with varying degrees of hydrophobicity, doped with Eu (III), namely MJ0_Eu, MJ2_Eu, MJ4_Eu, MJ6_Eu, and MJ8_Eu, are shown in Fig. 41. The luminescence of composite materials has been compared to that of the pure powdered luminescent complex [Eu(phen)2].(NO3)3. The well-known peaks of the europium ion emission are clearly observed at 5D0→7FJ (J=0-4): The transition 5D0→7F0 is the least intense at 580 nm. This transition is strongly prohibited by the selection rules. His presence indicates that the europium ion is not located at a center of symmetry [60].

Two close peaks can be seen in the region of the magnetic dipole transition 5D0→7F1, 585→600 nm. They may be due to the presence of several available species in the sample or to the splitting of Stark multiplets due to the low symmetry of the environment around the emitting ion. The most intense peak that gives the red color to europium luminescence is centered around 615 nm. It is due to the transition 5D0→7F2 and accounts for about 75% of the total intensity of the entire emission of the samples. The electric dipole transitions with ΔJ=2 are hypersensitive to their surrounding environment. Their intensity strongly depends on the symmetry of the ligands around the ion. The relative intensity between the electric dipole transition 5D0→7F2 and the magnetic dipole transition 5D0→7F1 (IED/IMD) is an indicator of a change in the structure of a given europium compound. Additionally, two peaks are observed in the regions 5D0-7F3 (645→655 nm) and 5D0→7F4. (675-685 nm).

The spectrum of the pure luminescent complex indicates symmetry around the europium ion C2V or lower. In the scratched samples, a strong non-homogeneous widening of the stripes is observed, which prevents the separation of different Stark multiplets (the resolution is about 1.5 nm). The presence of similar activating centers leads to very close overlapping peaks and a reduction in the resolution of the spectra. The structural changes in the luminescent complex in aerogel composites have been analyzed through the relative intensities IED/IMD and powder X-ray diffraction analysis.

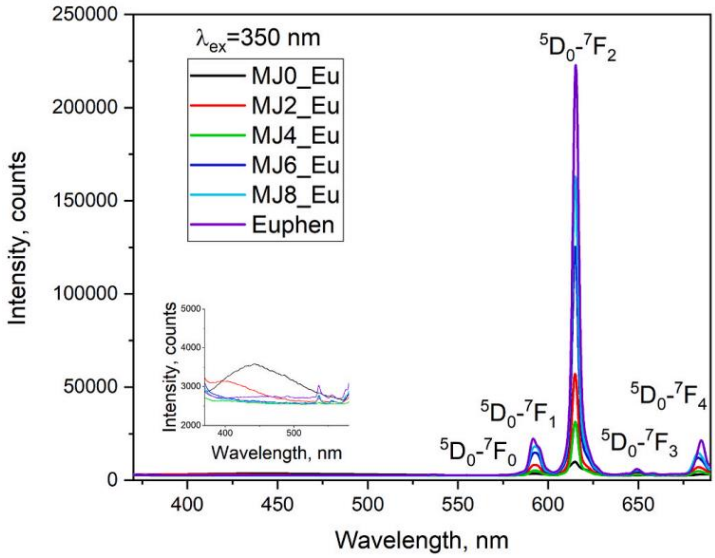

Fig. 41. Luminescent spectra of samples MJ0_Eu, MJ2_Eu, MJ4_Eu, MJ6_Eu и MJ8_Eu, excitation wavelength λ=350 nm.

It is noted that with the increase in the hydrophobicity of the matrix, the intensity of the emission increases and approaches that of the pure europium complex. In the hydrophilic sample MJ0_Eu and the weakly hydrophobic sample MJ2_Eu, a blue emission is also observed, the intensity of which is comparable to that of the europium emission. The maxima of these peaks are at 450 and 400 nm for the samples MJ0_Eu and MJ2_Eu. It is not observed in the spectra of the composites in the hydrophobic matrix (MJ4, MJ6, and MJ8) and the pure complex. This indicates an inefficient energy transfer between the ligand 1,10-phenanthroline and the activator ion Eu3+. For the energy transfer via Forster to be effective, the ligand and the metal must be close together and there must be spectral overlap.

In the hydrophilic matrices, there is likely a larger amount of water and solvents remaining, as well as many hydroxyl groups. These chemical inclusions can coordinate around metal ions and hinder their binding with the phenanthroline molecule. They also have high-energy quantum oscillators at 3000-3500 cm-1, through which the proportion of non-radiative relaxation increases, thereby further reducing the intensity of the emitted light. The blue emission from the ligand changes the final color of the emission of the composite materials.

The next figure (fig. 42) shows the emission spectra of the composites containing the complex [Tb(phen)2](NO3)3 and compares them with that of the pure component. In them, the well-known stripes for Tb (III) – 5D4→7FJ (J=6-0) are observed. The most intense transition is 5D4→7F5 at 542 nm, accounting for about 55% of the total emission intensity. The next most intense peak is at 580 nm – 5D4→7F6. Two multiplets are observed in the transition regions 5D4→7F4 (550-600 nm) and 5D4→7F3 (620-650 nm), along with one low-intensity peak at 650 nm (5D4→7F2). Again, the intensities follow a similar dependence; with the increase in the hydrophobicity of the matrix, the emission intensity increases and approaches that of the pure luminescent component.

The probes in matrices MJ0 and MJ2 have a blue emission from the ligand 1,10-phenanthroline. This again speaks to poor energy transfer or something that hinders the formation of the complex between the Tb (III) ion and the ligand.

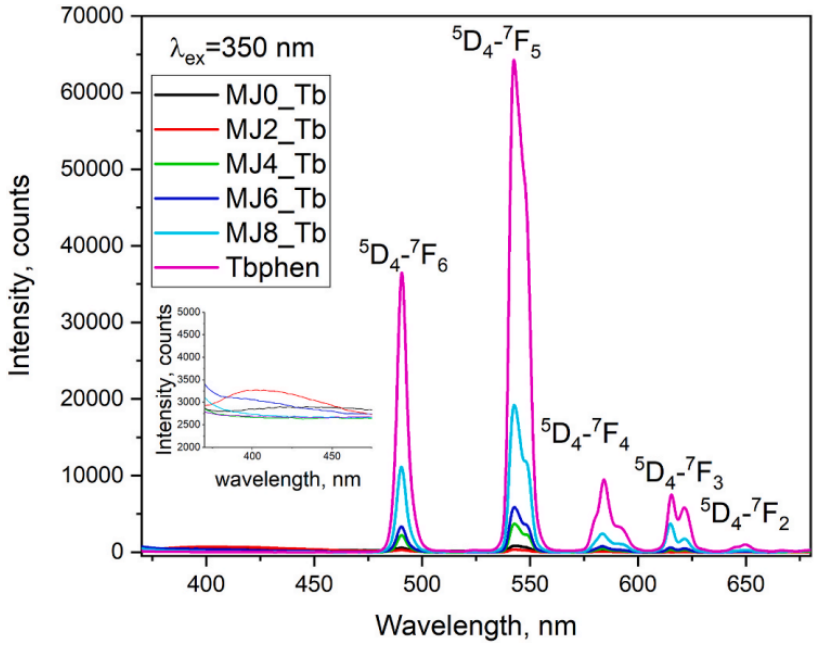

Fig. 42. Emission spectra of samples MJ0_Tb, MJ2_Tb, MJ4_Tb, MJ6_Tb и MJ8_Tb, containing the luminescent complex $[Tb(phen)_2](NO_3)_3$.

The mechanism of energy transfer between the ligand and the ions can be studied through the excitation spectra of the samples. The excitation spectra of the two series doped with Eu (III) and Tb (III) are shown in Fig. 43. They were recorded as the exciting radiation was changed between 200 and 400 nm, and the intensity of the most intense peaks in the samples was monitored. For the europium samples, this is the transition at 615 nm, and for those with terbium – 542 nm. The spectra are normalized to the highest recorded intensity for easier comparison. Three main channels are observed through which the rare earth ions are excited. The intense peak around 260 nm is likely associated with charge transfer transitions from the oxide matrix or coordinated nitrate anions around the ion [60]. The broad band in the range of 300-375 nm is due to the direct absorption of UV light by the ligand 1,10-phenanthroline. The low-intensity peak around 385 nm is a direct excitation of the rare earth ions. It has an intensity of about 10% of the most intense peak in the excitation spectrum. These are the transitions 5L6→7F0 for Eu (III) [92] and 5D3→7F6 for Tb (III) [93].

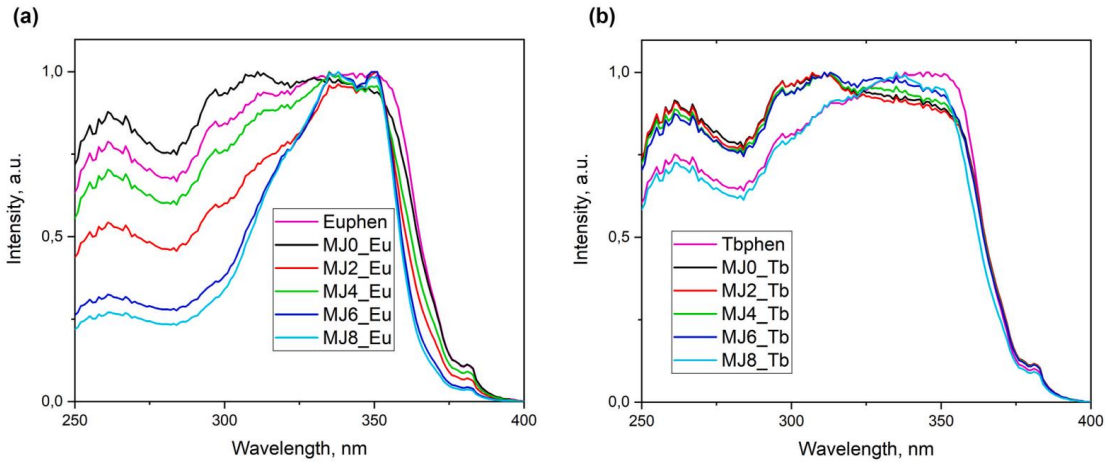

Fig. 43. Excitation spectra of a) samples containing the luminescent europium complex [Eu(phen)2](NO3)3: MJ0_Eu, MJ2_Eu, MJ4_Eu, MJ6_Eu, and MJ8_Eu, as well as the pure complex Euphen; b) samples containing the terbium complex - [Tb(phen)2].(NO3)3: MJ0_Tb, MJ2_Tb, MJ4_Tb, MJ6_Tb, MJ8_Tb, and the pure luminescent complex Tbphen.

The observed bands in the excitation spectrum are well explained by the familiar mechanisms of energy transfer in complex compounds. The broad band of the transition with charge transfer (260 nm) is due to the transition via the Dexter mechanism. An electron from the ligand is excited and transitions to the orbital of the metal ion, thereby reducing it, while an electron from the ground state of the metal ion jumps to a low-energy orbital of the ligand. These types of transitions are allowed according to the selection rules and always appear as broad, intense stripes. Their position strongly depends on the electronegativity of the ligands. In oxide matrices or in the presence of oxygen-containing ligands, the transition O2- → Ln3+ is centered around 260 nm. If the ligands are more electronegative, such as fluoride anions F-, as in fluoride ceramics and glasses, the maximum of the transition with the transfer of this can have a blue shift of up to 200 nm [94]. The internal f-f transitions in rare earth ions are forbidden according to selection rules. For this reason, the peak around 390 nm appears with a very low relative intensity compared to the other transitions. The transitions with charge transfer have molar absorptivities on the order of 10^4 L/mol.cm, while f-f transitions are less than 100 [95].

The other intense peak in the range of 300-375 nm is due to absorption by the organic ligands around the metal ion. The π-π* transitions in organic molecules have intensities comparable to charge transfer transitions (10^4 L/mol.cm). The mechanism of energy transfer is the well-known Förster resonance energy transfer.

The energy transfer in the complex [Tb(phen)2](NO3)3 and other similar compounds has been thoroughly investigated using experimental and theoretical approaches by Ts. Zahariev and co-authors [55,88,96]. The diagram is shown in Fig. 44. After a photon is absorbed by the ligand and it transitions from the ground state S0 to an excited state S1, and sometimes even higher states S2 or S3, it can relax through fluorescence back to the ground state and emit a photon. Triplet states are always lower in energy than excited singlet states, so the ligand can relax from an excited singlet state to a triplet state S1→T1. These types of transitions are forbidden in spin, and the

system can remain in a triplet state, from where it can relax to S0 through phosphorescence and emit a photon. It is known that the energy of the triplet state of the ligand is of great importance for the efficiency of energy transfer to the metal ion. If T1 is located 1000-2000 cm-1 above the excited state of the metal ion (spectral overlap – resonance in the energy levels), it is possible for the energy to be transferred to the metal ion, which upon relaxation can emit a photon in the visible region.

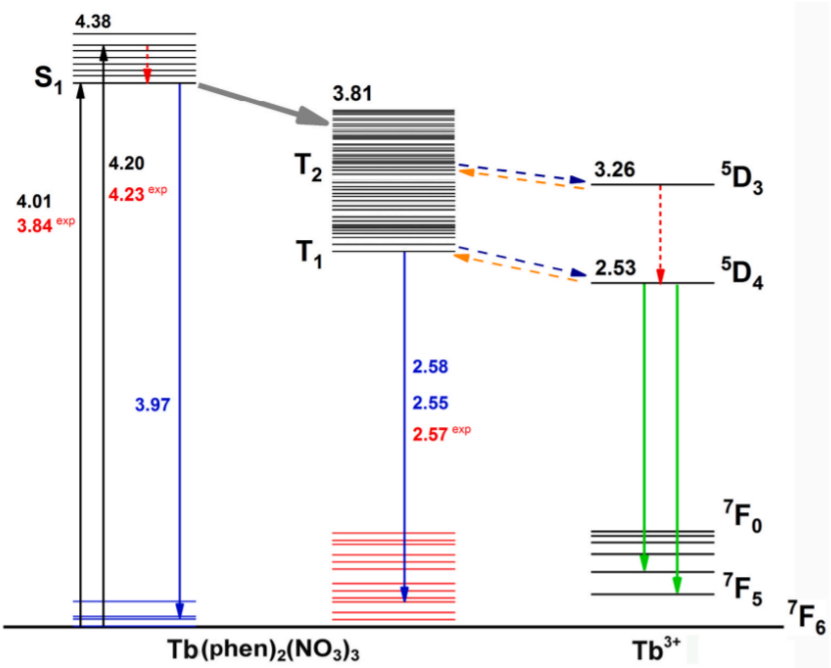

Fig. 44. Scheme for the energy transfer pathway from 1,10-fenanthroline to the metal ion Tb (III).

A number of phenomena can lead to a decrease in the efficiency of the luminescence of a given material. If the energy of the triplet state of the ligand T1 is too close to the excited state of the metal ion, significant back energy transfer may be observed due to thermal fluctuations. Poor spectral overlap and structural defects that lead to a greater distance between the ligands and the metal center reduce the efficiency of energy transfer. The presence of water molecules, other solvents, or unreacted –OH groups from the matrix may facilitate non-radiative relaxation, as these types have high-energy vibrations. If a system can relax by emitting 5-6 phonons or fewer, it is likely that this path will be preferred over the emission of a high-energy photon from the visible or ultraviolet region [45]. These data were obtained by applying perturbation theory for systems that relax through different numbers of phonons and photons, and the probability for the various transitions has been determined. The energy separated by phonons can be detected as an increase in the temperature of the matrix. Water molecules have high-energy vibrations with energy ranging from 3000 to 3800 cm-1. Five to six phonons with this energy fall within the range of 440-670 nm. From here, it can be observed that in order to achieve an effective luminescent material, a suitable ligand for the corresponding metal ion must be carefully selected, and the luminescent center should be protected from various external influences and moisture.

The efficiency of a luminescent material can be assessed by its quantum yield. (QY). This is the ratio of emitted to absorbed photons. The absolute quantum yield of the complex [Eu(phen)2](NO3)3 is 35%, while that of [Tb(phen)2](NO3)3 is 13%. This shows that the phenanthroline molecule is a more effective antenna for the europium ion. In this case, this is most likely due to the energies of the triplet state of the ligand and the excited states of the ions. The excited state 5D4 of Tb3+ is closer in energy to T1 of phenanthroline than to the 5D0 level of the Eu3+ ion. Figure 45 shows how the quantum yield of luminescent composite materials changes with their degree of hydrophobicity α. In both series, the one doped with [Eu(phen)2](NO3)3 and the one with [Tb(phen)2](NO3)3, an increase in quantum yield is observed with the degree of hydrophobicity of the matrix. The probes MJ0_Eu, MJ2_Eu, MJ4_Eu, MJ6_Eu, and MJ8_Eu have quantum yields of 5.72%, 18.26%, 24.67%, 27.67%, and 31.42%, respectively. A monotonous increase in quantum yield is observed, and the strongly hydrophobic sample MJ8_Eu has a quantum yield comparable to that of the pure component. The quantum yield of the blue light emitted by the sample MJ0_Eu is 3.03%. Which makes it more than half of the entire sample emission. The composite materials doped with terbium complex have a lower quantum yield. The measured quantum yields for samples MJ0_Tb, MJ2_Tb, MJ4_Tb, MJ6_Tb, and MJ8_Tb are 1.57%, 1.18%, 11.02%, 5.66%, and 10.46%, respectively, while the quantum yield of the blue emission in samples MJ0_Tb and MJ2_Tb is 1.18% and 1.07%. The newly obtained properties are again lower than those of the pure luminescent complex [Tb(phen)2](NO3)3, but the highly hydrophobic sample MJ8_Tb has an efficiency close to that of the pure complex. In this series, however, the blue emission for the hydrophilic (MJ0_Tb) and weakly hydrophobic (MJ2_Tb) samples is more than 2/3 of the total luminescence intensity. The error in this type of measurements is about 5%.

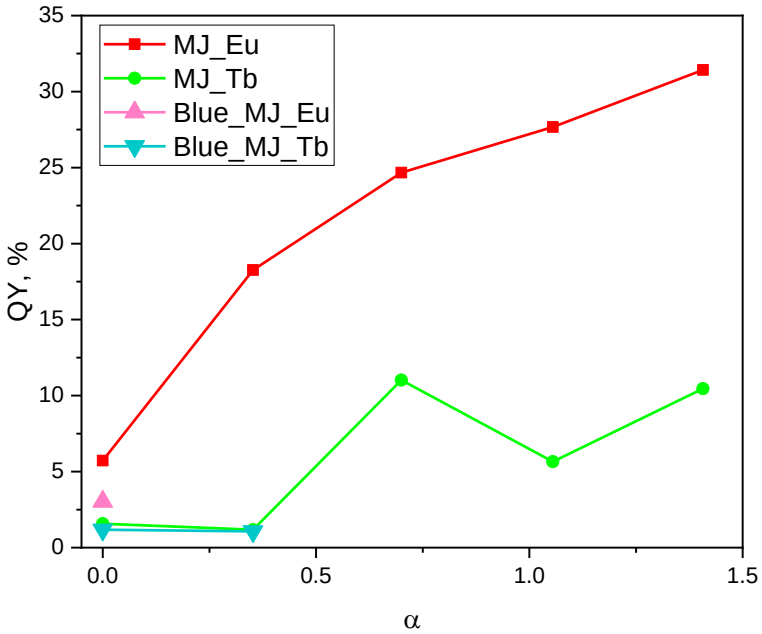

Fig. 45. Measured absolute quantum yields of composite materials as a function of hydrophobicity degree α. The samples containing the complex [Eu(phen)2](NO3)3 are marked with a red line (MJ_Eu), while the samples with [Tb(phen)2](NO3)3 are marked in green (MJ_Tb). The relative share of blue luminescence in the samples where it was observed is shown.

From the measured absolute quantum yields of the obtained luminescent composite materials, it can be concluded that the matrix has a strong influence on the efficiency of energy transfer between the ligand and the lanthanide ion. Overall, the quantum yield increases with the increase in the hydrophobicity of the matrix. The removal of remaining water molecules and unreacted hydroxyl groups from the matrix reduces the proportion of non-radiative relaxation by decreasing the phonon energy of the matrix and stimulating radiative relaxation – through photons in the visible range. This, in our opinion, is the main reason for the description of the first-time effect.

The blue emission observed in the hydrophilic samples MJ0Eu, MJ0_Tb, and MJ2_Tb indicates incomplete formation of the complex between phenanthroline and the ions. Other authors also find that when the energy transfer between the ligand and the ion is weak or somehow obstructed, emission is observed from the ligands instead of the ions. This occurs with weak spectral overlap or with steric hindrance, which prevents the complete formation of the complex.

4.2.4 XRD – structural changes in the composite materials.

The structure of the obtained composite materials has been investigated using spectroscopic methods and X-ray structural analysis. The X-ray images were taken using a Siemens D 500 diffractometer, with a step of 0.05º and 2 seconds per step. Cu Kα radiation has been used. The analysis of the X-rays was conducted using the computer program Powdercell [97]. A qualitative X-ray phase analysis has been conducted; due to the low concentrations of the doping impurity, a quantitative analysis is not possible. Theoretical X-ray diffraction patterns of pure luminescent components (Euphen, Tbphen, and phen) have been simulated from data taken from experimental CIF files. The following data has been used: [Eu(phen)2](NO3)3 – CCDC 154103; [Tb(phen)2](NO3)3 - CCDC 169824; solid 1,10 – phenanthroline – CCDC 154103. Additionally, the theoretical X-ray diffractograms were constructed from crystallographic data for Eu(NO3)3 and Tb(NO3)3, as well as their possible crystal hydrates, to verify their presence in the obtained composites.

The two luminescent complexes of europium and terbium are isostructural with slight differences in the parameters of the crystal lattice. The structure of the terbium complex is shown in Figure 47. Both compounds have a monoclinic crystal lattice with a space group C 2/c (number 15). The parameters of the crystal lattice of the europium complex are a=11.1650(10) Å, b=17.972(2) Å, c=13.0520(10) Å, α=90°, β=100.565(7)°, γ=90°, while those of the terbium complex are a=11.1550(10) Å, b=17.914(2) Å, c=13.0260(10) Å, α=90°, β=100.549(9)°, and γ=90°. The volume of the elementary cell of the complex [Eu(phen)2](NO3)3 is 2574.6(4) Å3, while that of the terbium complex is 2559.0(4) Å3, which follows the sizes of the ionic radii of the

metal ions. Europium (III) has an ionic radius of 108.7 pm, while Terbium (III) has an ionic radius of 106.3 pm.

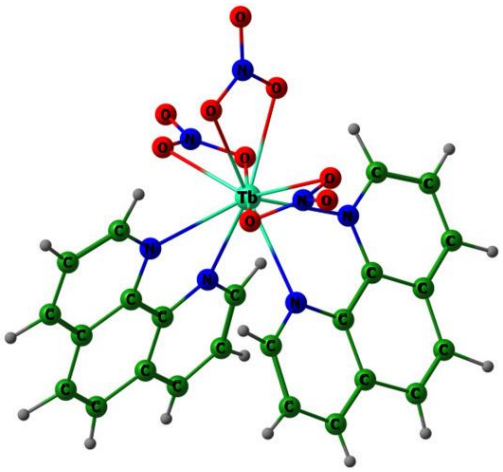

Fig. 47. Structure of the complex $[Tb(phen)_2](NO_3)_3$.

The spectroscopic structure of hybrid complexes can be investigated by analyzing the positions of the peaks and the number of Stark multiplets observed for each luminescent or absorption peak. For the pure luminescent components, it turns out that the environment around the rare earth ions has C2v symmetry or lower. In the obtained composites, a strong inhomogeneous broadening of the peaks is observed due to the presence of many similar species with small differences in structure. This does not allow for the precise determination of the Stark multiplets at each peak, especially for the low-intensity peaks.

The presence of lines close to each other at the available resolution (1.5 – 2 nm) of the obtained spectra leads to broad stripes. Therefore, another criterion was used for the analysis of symmetry, namely the ratio of the intensities of the most intense electric dipole peak to the magnetic dipole peak. For [Eu(phen)2](NO3)3, the IED/IMD ratio was used from the transitions 5D0-7F2 and 5D0-7F2, while for the terbium complex, the intensities of the transitions 5D4–7F6 and 5D4–7F5 were used. The developed procedures for analyzing the symmetry around the europium ion clearly indicate that an increase in the IED/IMD ratio means that symmetry decreases [60]. In a crystal where the europium ion is located at a center of symmetry, this ratio IED/IMD<1, meaning the magnetic dipole transition 5D0-7F1 is more intense. There are no established procedures for determining the symmetry of the environment around the ion, but changes in the relative intensities of the peaks indicate that structural changes in the crystals are also being observed. For the pure luminescent complexes [Eu(phen)2](NO3)3 and [Tb(phen)2](NO3)3, the IED/IMD ratios were measured to be 7.25 and 0.37, respectively. The calculated intensity ratios for the obtained luminescent composite materials are summarized in Fig. 48, as a function of the hydrophobicity degree of the matrix. The trend is an increase in the intensity ratio IED/IMD as the hydrophobicity of the matrix increases. For the europium complex, it changes within the range of 5.7-7, while for the terbium complex, it is between 0.4-0.5. These values indicate a low symmetrical environment around the ions. The significant differences in intensity relationships

indicate that there are structural differences in the luminescent components depending on the matrix. More direct structural information can be obtained from the X-rays of the samples.

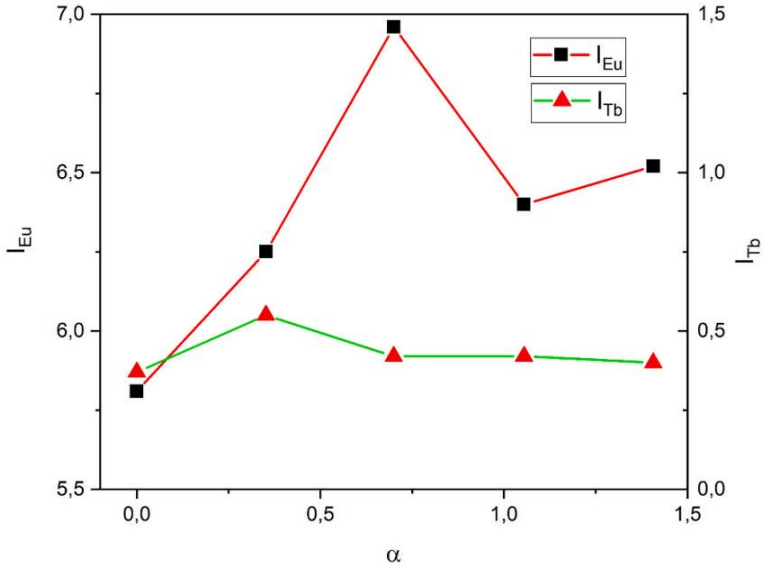

Fig. 48. Intensity relationships IED/IMD for the obtained luminescent composite materials as a function of the hydrophobicity degree of the matrix.

The obtained composites doped with 0.35% luminescent complex are X-ray amorphous, which is why composites with 1% dopant were synthesized using the same procedure in order to observe the X-ray peaks of the doping impurity. Figure 49 shows the taken X-rays. The average size of the crystallites, calculated using the Scherrer formula, for the pure complexes is about 50 nm.

The same calculations for the average sizes of the crystallites of the incorporated complexes in a silicate matrix undoubtedly show a reduction in size to 25 nm. This is most likely due to limitations caused by the small size of the pores in the gels. An analysis has been conducted and it has been established that the most intense peaks of Eu(NO3)3 and Tb(NO3)3, as well as their possible crystal hydrates, are absent in the X-ray images of the obtained composites. Peaks of nanocrystalline 1,10-phenanthroline have been observed, marked with # figure 49. This demonstrates the effectiveness of the developed procedure for functionalizing aerogel granules and the complete conversion of Eu(NO3)3 and Tb(NO3)3 into Eu(phen)2(NO3)3 and Eu(phen)2(NO3)3.

Similarly, in spectral analysis, the relative intensities and positions of the peaks in the X-ray patterns of the composites indicate structural changes occurring during the in situ formation of the complexes. The optical properties of composite materials with 1% luminescent complex are similar to those of materials containing 0.35%. The quantum yields of samples MJ4_0.1Eu and MJ4_0.1Tb are 32% and 11%, respectively.

The analysis of the X-rays shows that the interplanar distance d-112 decreases by about 0.6-0.8% due to the growth of the crystallites of the complex in a silicate matrix compared to the

pure components. Also, the reflections at 2θ = 22.4° (hkl = 132); 23.16° (hkl = 202); 24.11° (hkl = 042, 113) are shifted to higher values compared to those in the pure complexes. This can be explained by the presence of structural defects (disorder) in the activator phase, which occur under conditions far from equilibrium. The presence of texture in the pores of the matrix is also possible, but it would not lead to a change in interlayer distances.

Another possibility is the formation of various polymorphic forms of the pure complexes [Eu(phen)2](NO3)3 and [Tb(phen)2](NO3)3 [86,98]. A recent study shows that the complex [Eu(phen)2](NO3)3 can crystallize in two different monoclinic structures depending on the conditions and the method used to obtain the complex [99]. A complete structural characterization of the obtained samples is very difficult due to the low concentrations of dopant and the presence of an amorphous matrix.

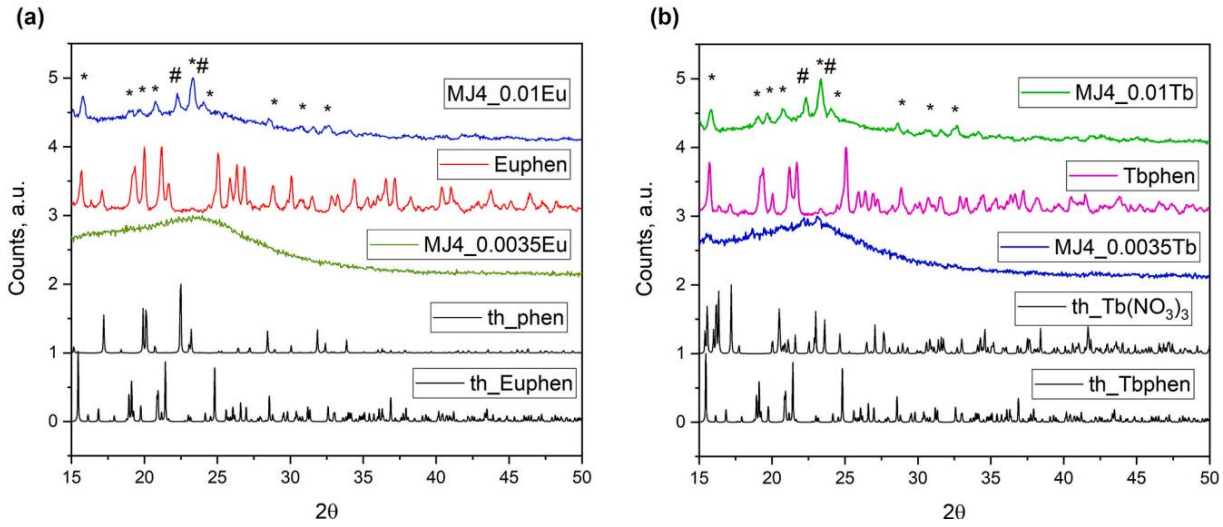

Fig. 49. X-rays of luminescent composites and pure components. The constructed theoretical X-ray patterns of pure luminescent complexes, as well as the nitrates of europium and terbium (denoted as th_formula), and pure 1,10-phenanthroline (th_phen) are presented. The peaks of the pure complexes are marked with *, those of the traces of 1,10-phenanthroline are marked with #.

5 Conclusions

1. A successful laboratory-scale, subcritical procedure has been developed for obtaining hydrophobic silica aerogels at room temperature, with powders having a specific surface area of 800–1000 m^2/g, an average pore diameter of 5–10 nm, and a density of 0.2-0.3 g/cm^3.

2. Анализът на относителните интензитети на ATR-IR пиковете на SiO2 в интервала 900 – 1300 cm-1 е ефективен метод за проследяване на повърхностната хидрофобизация на силикатни прахове с TMCS. The relative intensity of the □as(Si-OH) ATR-IR peak of SiO2 decreases upon hydrophobization, which correlates with the increase in the relative intensity of the □s(Si-CH) peaks. The process is accompanied by the rearrangement of four- and six-membered siloxane rings in the aerogel matrix.

3. The textural properties of the obtained aerogel silicate micropowders depend on their degree of hydrophobicity. The analysis of the adsorption isotherms of nitrogen on these materials at 77 K leads to a calculated fractal coefficient Ds = 2.80–2.50, as well as evidence for the existence of two types of nanopores: bottle-shaped and disk-shaped.

4. The nanocomposites obtained through a two-step functionalization procedure with the composition SiO2:[Ln(phen)2](NO3)3; (Ln = Eu, Tb) represent an amorphous, hydrophobic matrix in which nanocrystals of [Ln(phen)2](NO3)3 are embedded, with an average size of 20-30 nm.

5. The optical properties (emission spectra, excitation, and quantum yield) of aerogel nanocomposites depend on the degree of hydrophobicity of the starting aerogel matrix. The luminescence of the obtained materials is dominated by the presence of energy transfer 1,10-phenanthroline→Ln3+ and transitions involving charge transfer O2-→Ln3+.

6. The quantum yield of hybrid composites increases with their degree of hydrophobicity, reaching the values of the pure [Ln(phen)2](NO3)3 complex at alpha = 1.5. The reason for this increase lies in the chemical reaction of hydrophobization, leading to the removal of surface -OH groups.

7. The analysis of the luminescent spectra of hybrid nanocomposites demonstrates the change in symmetry and chemical bonding at the molecular level of the complex [Ln(phen)2](NO3)3 when embedded in the aerogel matrix. This result correlates with X-ray structural data indicating the presence of structural polymorphism in [Ln(phen)2](NO3)3.

8. The obtained hydrophobic aerogel composites have increased thermal stability compared to classical sol-gel materials. The functionalization with [Ln(phen)2](NO3)3, (Ln = Eu, Tb) nanocrystals does not significantly change the textural properties of the hydrophobic aerogel granules. The physical properties of the obtained nanocomposites are favorable for the development of luminescent sensors based on them.

6 Contributions

- For the first time, the hydrophobization of amorphous silicon dioxide has been quantitatively described through the analysis of ATR/IR spectra in the range of 900 - 1300 cm-1, and the formation of nanopores with different shapes during the hydrophobization of silicon dioxide with TMCS has been demonstrated.

- A physicochemical methodology has been published for the functionalization of silicate aerogel garnets with complexes of [Ln(phen)2](NO3)3; Ln = Eu, Tb.

- The intention is to investigate the dependence of the optical properties (emission spectra, excitation, and quantum yield) of aerogel nanocomposites SiO2: [Ln(phen)2](NO3)3; Ln = Eu, Tb on the degree of hydrophobicity of the starting matrix.

- Differences in the microstructure of the pure complexes [Ln(phen)2](NO3)3 and the composites SiO2: [Ln(phen)2](NO3)3 are shown, as well as the presence of structural polymorphism.

- Increased thermal stability of the obtained hybrid aerogel composites has been demonstrated compared to classical sol-gel composites.

- The aerogel nature of the obtained composites has been proven, a property suitable for the development of luminescent sensors.

7 Publications containing results from the dissertation.

1. D. Shandurkov, P. Ignatov, I. Spassova, S. Gutzov, Spectral and Texture Properties of Hydrophobic Aerogel Powders Obtained from Room Temperature Drying, Molecules 26 (2021) 1796 https://doi.org/10.3390/molecules26061796.
2. S. Gutzov, D. Shandurkov, N. Danchova, V. Petrov, T. Spassov, Hybrid composites based on aerogels: preparation, structure and tunable luminescence, J. Luminescence, 251 (2022) 119171. https://doi.org/10.1016/j.jlumin.2022.119171
3. D. Shandurkov, N. Danchova, S. Gutzov, Functional optical materials based on aerogels, Journal of Chemical Technology and Metallurgy, 2024 (in press), doi:10.59957/jctm.v59.i6.2024.XX
4. S. Gutzov, D. Shandurkov, N. Danchova, Aerogels – new materials with promising applications, e-Proceedings of the International scientific conference UNITECH 2021, 18.11 –19.11.2021, Gabrovo, https://unitech-selectedpapers.tugab.bg/images/papers/2021/UnitechSP_2021.pdf

8. Participation with presentations at conferences, including results from the dissertation.

1. Димитър Шандурков, Н. Данчова, В. Петров, С. Гуцов, „Луминесцентни нанокомпозитни материали: получаване, структура и свойства“, XXI НАЦИОНАЛНА КОНФЕРЕНЦИЯ ПО ХИМИЯ ЗА СТУДЕНТИ И ДОКТОРАНТИ, 17-19 май 2023 г. СОФИЯ.
2. Dimitar Shandurkov, Nina Danchova, Vesselin Petrov, Stoyan Gutzov, New Sol-Gel Composite Materials With Multicolour Emission: Physicochemical and Luminescent Properties, 8th International Sol-Gel Society Workshop SUSGEM 2023: SUSTAINABLE SOL-GEL ENERGY MATERIALS, 01-04 October 2023, Castelló (Spain).
3. Stoyan Gutzov, Dimitar Shandurkov, Nina Danchova, Functional optical materials, based on aerogels, 8. Balkan Conference on Glass Science and Technology, 25.09-27.09. 2023, Nessebar, Bulgaria.
4. Димитър Шандурков, Стоян Гуцов, Веселин Петров, Нови композитни материали с многоцветна емисия: физикохимични и оптични свойства, Белчин, 16-18 октомври, 2023

9. Noted citation of publications related to the disertation

Molecules (2021) (SCOPUS)

1. Park, J., Jeong, M., Cho, Y.J., Kim, K.J., Tai, T.B., Shin, H., Lim, J.C., Chang, H.S., Investigation of tetrakis(ethylmethylamido)hafnium adsorption mechanism in initial growth of atomic layer deposited-HfO2 thin films on H-/OH-terminated Si (100) surfaces (2023), Journal of Vacuum Science and Technology B, 41 (6), art. no. 062801 .
2. Yahya, E.B., Elarbash, S.S., Ben Moussa, S., Hajri, A.K., Abdullah Alzahrani, A.Y., Khalil, H.P.S.A., Microbial assisted date palm nanocellulose isolation and the fabrication of hydrophobic bioaerogel for oil absorption application, (2024) Industrial Crops and Products, 221,
3. Liu, B., Sun, L., Jin, F., Wan, Y., Han, X., Fu, T., Guan, Y., Xie, Z., Cheng, L., Tian, B., Feng, Z., A novel oleogel based on porous microgel from egg white, (2023) Food Hydrocolloids, 144, art. no. 109049.
4. Li, Z., Wang, Y., Wu, X., Liu, Q., Li, M., Shi, L., Cheng, X., Surface chemistry, skeleton structure and thermal safety of methylsilyl modified silica aerogels by heat treatment in an argon atmosphere , (2023) Journal of Non-Crystalline Solids, 611, art. no. 122335.

J. Luminescence (2022) SCOPUS

5. Synthesis, crystal structure and luminescence properties of two novel Tb (III) complexes with 1, 10-phenanthroline derivatives as ligands, M Tsvetkov, D Elenkova, M Kolarski, R Lyapchev et al - Journal of Molecular Structure, 1314 (2024) 138768

6. Scanda K, Salas-Juárez CJ, Guzmán-Silva RE, Beltran HI, Garduño I, Guzmán-Mendoza J. Synthesis and photoluminescent spectroscopic analysis of lanthanum (III) coordinated with 1,10-Phenanthroline: A study of its thermally stable behavior. Spectrochim Acta A Mol Biomol Spectrosc. 2024; 325:125046. doi: 10.1016/j.saa.2024.125046.

10. Bibligraphy.

1. KISTLER, S.S. Coherent Expanded Aerogels and Jellies. *Nature* **1931**, *127*, 741, doi:doi:10.1038/127741a0.

2. KISTLER, S.S. Coherent Expanded-Aerogels. *J. Phys. Chem.* **1932**, *36*, 52–64, doi:DOI: 10.1021/j150331a003.

3. GA, N.; SJ, T. Preparation of silica aerogels from methyl orthosilicate in alcoholic medium, and their properties. *Bull Soc Chim Fr* **1968**, 1906–1911.

4. Teichner, S.J. Aerogels of Inorganic Oxides. *Springer Proc. Phys.* 1986, 22–30.

5. Brinker, C.J.; Ward, K.J.; Keefer, K.D.; Holupka, E.; Bray, P.J.; Pearson, R.K.; CJ, B.; KJ, W.; KD, K.; E, H.; et al. Synthesis and structure of borate based aerogel. *Springer Proc Phys* **1986**, *6*, 57–67, doi:10.1007/978-3-642-93313-4_7.

6. RW, P.; ST, M.; JL, K.; FM, K.; Pekala, R.W.; Mayer, S.T.; Kaschmitter, J.L.; Kong, F.M. Carbon aerogels: an update on structure, properties, and applications. *Sol-gel Process Appls* **1994**, 369–377, doi:10.1007/978-1-4615-2570-7_32.

7. Pekala, R.W.; RW, P. Organic aerogels from the polycondensation of resorcinol with formaldehyde. *J Mater Sci* **1989**, *24*, 3221–3227, doi:10.1007/bf01139044.

8. Aegerter, M.A.; Leventis, N.; Koebel, M.M. *Aerogels Handbook*; Springer: New York, 2011;

9. Livage, J.; Henry, M.; Sanchez, C. Sol-Gel Chemistry of Transition Metal Oxides. *Prog. Solid State Chem.* **1988**, *18*, 259–341.

10. Soleimani, Д.; Abbasi, M.; Soleimani Dorcheh, A.; Abbasi, M.H. Silica aerogel; synthesis, properties and characterization. *J Mater Proc Technol* **2008**, *199*, 10–26, doi:10.1016/j.jmatprotec.2007.10.060.

11. MA, E.; E, N.; A, R.; GM, P.; S, B.; D, V.; M, D.; P, C.; P, N.; F, E.-D.; et al. Strengthening of silica gels and aerogels by washing and aging processes. *J. Non-Cryst* **2001**, *285*, 1–7, doi:10.1016/s0022-3093(01)00423-9.

12. Venkateswara Rao, A.; Haranath, D.; A, V.R.; D, H. Effect of methyltrimethoxysilane as a synthesis component on the hydrophobicity and some physical properties of silica aerogels. *Microporous Mesoporous Mater* **1999**, *30*, 267–273, doi:10.1016/s1387-1811(99)00037-2.

13. Zhou, B.; Shen, J.; Wu, Y.; Wu, G.; Ni, X.; B, Z.; J, S.; W, Y.; G, W.; X, N.; et al. Hydrophobic silica aerogels derived from polyethoxydisiloxane and perfluoroalkylsilane. *Mater Sci Eng C* **2007**, *27*, 1291–1294, doi:10.1016/j.msec.2006.06.032.

14. M, M.-G.; A, R.; E, M. Sol-Gel Route to Direct Formation of Silica Aerogel Microparticles

Using Supercritical Solvents. *J Sol Gel Sci Technol* **2003**, *26*, 645–649.

15. Venkateswara Rao, A.; Bhagat, S.D.; Hirashima, H.; Pajonk, G.M.; A, V.R.; SD, B.; H, H.; GM, P. Synthesis of flexible silica aerogels using methyltrimethoxysilane (MTMS) precursor. *J Colloid Interface Sci* **2006**, *300*, 279–285, doi:10.1016/j.jcis.2006.03.044.

16. Mezza, P.; Phalippou, J.; Sempere, R. Sol–gel derived porous silica films. *J Non-Cryst Solids* **1999**, *243*, 75–79.

17. Dieudonné, P.; Alaoui, A.H.; Delord, P.; Phalippou, J.; P, D.D.; A, H.A.; P, D.D.; J, P. Transformation of nanostructure of silica gels during drying. *J Non-Cryst Solids* **2000**, *262*, 155–161, doi:10.1016/s0022-3093(99)00687-0.

18. M-A, E.; MB, K.; E, N.; K, M.; J, S. Einarsrud M-A, Kirkedelen MB, Nilsen E, Mortensen K, Samseth J. *J Non-Cryst Solids* **1998**, *231*, 10–16.

19. A, V.R.; MM, K.; GM, P.; DP, A.; T, S. Synthesis and Characterization of Hydrophobic Silica Aerogels Using Trimethylethoxysilane as a Co-Precursor. *J Sol Gel Sci Technol* **2003**, *23*, 103–109.

20. Shandurkov, D.; Ignatov, P.; Spassova, I.; Gutzov, S. Spectral and Texture Properties of Hydrophobic Aerogel Powders Obtained from Room Temperature Drying. *Molecules* **2021**, *26*, 1796, doi:10.3390/molecules26061796.

21. Gutzov, S.; Danchova, N.; Kirilova, R.; Petrov, V.; Yordanova, S. Preparation and luminescence of silica aerogel composites containing an europium (III) phenanthroline nitrate complex. *J. Lumin.* **2017**, *193*, 108–112, doi:doi:10.1016/j.jlumin.2016.11.029.

22. Petkova, N.; Gutzov, S.; Lesev, N.; Kaloyanova, S.; Stoyanov, S.; Deligeorgiev, T. Preparation and optical properties of silica gels doped with a new Eu (III) complex. *Opt. Mater. (Amst).* **2011**, *33*, 1715–1720.

23. Song, Y.; Li, B.; Yang, S.; Ding, G.; Zhang, C.; Xie, X. Ultralight boron nitride aerogels via template-assisted chemical vapor deposition. *Sci. Rep.* **2015**, *5*, 10337, doi:10.1038/srep10337.

24. L, K.; F, D.; J, P.; Kocon, L.; Despetis, F.; Phalippou, J. Ultralow density silica aerogels by alcohol supercritical drying. *J Non-Cryst Solids* **1998**, *225*, 96–100, doi:10.1016/s0022-3093(98)00322-6.

25. Danchova, N.; Paskalev, D.; Gutzov, S. Aerogels – new materials with promising applications. *Bulg. Chem. Commun.* **2018**, *50*, 172–177.

26. Gutzov, S.; Danchova, N.; Karakashev, S.I.; Khristov, M.; Ivanova, J.; Ulbikas, J. Preparation and thermal properties of chemically prepared nanoporous silica aerogels. *J. Sol-Gel Sci. Technol.* **2014**, *70*, 511–516, doi:10.1007/s10971-014-3315-7.

27. Yoldas, B.E.; Annen, M.J.; Bostaph, J.; BE, Y.; MJ, A.; J, B. Chemical engineering of aerogel morphology formed under nonsupercritical conditions for thermal insulation. *Chem Mater* **2000**, *12*, 2475–2484, doi:10.1021/cm9903428.

28. B, W.; G, S.; FE, K. Thermal insulators having density 0.1 to 0.4 g/cm3, and their manufacture BASF-G. *Eur Pat Appl EP* **1989**.

29. D, Q.; B, C.; H, S.; F, O.; D, G. Heat transfer by conduction and radiation in building materials: review and new developments. *Rev Met. Cah. Inf Tech* **1998**, *95*, 1149–1158.

30. Blasse, G.; Grabmaier, B.C. *Luminescent Materials*; Springer-Verlag: Telos, 1994;

31. Stuart, B.H.; George, B.; McIntyre, P. *Modern Infrared Spectroscopy 2nd Edition*; Wiley, 1996;

32. Ball, D.W. Modern Spectroscopy, 4th ed. J. Michael Hollas. New York: John Wiley & Sons, Inc., 2004, 428 pp., $45.00, paperback. ISBN 0-470-84416-7. *Clin. Chem.* **2004**, *50*, 2469–2470, doi:10.1373/clinchem.2004.033902.

33. Workman, J.; Weyer, L. *Practical Guide to Interpretive Near-Infrared Spectroscopy*; CRC Press Taylor & Francis Group, 2008; ISBN 13: 978-1-57444-784-2.

34. Gunde, M.K. Vibrational modes in amorphous silicon dioxide. *Phys. B* **2000**, *292*, 286}295.

35. Tran, T.N.; Pham, T.V.A.; Le, M.L.P.; Nguyen1, T.P.T.; Tran, V.M. Synthesis of amorphous silica and sulfonic acid functionalized silica used as reinforced phase for polymer electrolyte membrane. *Adv. Nat. Sci. Nanosci. Nanotechnol.* **2013**, *4*, 6, doi:10.1088/2043-6262/4/4/045007.

36. Galeener, F.L. Band limits and the vibrational spectra of tetrahedral glasses. *Phys. Rev. B* **1979**, *19*, 4292–4297, doi:10.1103/PhysRevB.19.4292.

37. Galeener, F.L.; Lucovsky, G. Longitudinal optical vibrations in glasses: GeO2 and SiO2. *Phys. Rev. Lett.* **1976**, *37*, 1474–1478, doi:10.1103/PhysRevLett.37.1474.

38. Fidalgo, A.; Ilharco, L.M. Chemical Tailoring of Porous Silica Xerogels: Local Structure by Vibrational Spectroscopy. *Chem. – A Eur. J.* **2004**, *10*, 392–398, doi:10.1002/chem.200305079.

39. Sen, P.N.; Thorpe, M.F. Phonons in AX2 glasses: From molecular to band-like modes. *Phys. Rev. B* **1977**, *15*, 4030–4038, doi:10.1103/PhysRevB.15.4030.

40. Innocenzi, P. Infrared spectroscopy of sol–gel derived silica-based films: a spectra-microstructure overview. *J. Non. Cryst. Solids* **2003**, *316*, 309–319.

41. Characterization, S.; Catauro, M.; Barrino, F.; Poggetto, G.D.; Crescente, G.; Piccolella, S.; Pacifico, S. New SiO 2 / Ca ff eic Acid Hybrid Materials : Synthesis ,. **2020**, 1–12.

42. Fidalgo, A.; Ciriminna, R.; Ilharco, L.M.; Pagliaro, M. Role of the alkyl-alkoxide precursor on the structure and catalytic properties of hybrid sol-gel catalysts. *Chem. Mater.* **2005**, *17*, 6686–6694, doi:10.1021/cm051954x.

43. Thorpe, M.F.; Leeuw, S.W. de Coulomb effects in disordered solids. *Phys. Rev. B* **1986**, *33*, 8490 – 8505.

44. Bartolo, B. Di *Optical Interactions in Solids*; Boston College, 2010;

45. Henderson;, B.; Imbusch, G.F. *Optical Spectroscopy of Inorganic Solids*; Oxford, 1989; ISBN 0198513720.

46. Atkins, P.; Paula, J. de; Keeler, J. *Atkins' Physical Chemistry*; Oxford University Press (OUP), 2022; ISBN 9780198847816.

47. Тютюлков, Н. *Квантова химия*; Наука и изкуство: София, 1978;

48. Hull, R.; R. M. Osgood, J.; Paris!, J.; Warlimont, H. *Spectroscopic properties of Rare Earths in Optical Materials*; Springer, 2014; ISBN 3540238867.

49. Atkins, P.W. *Quanta: A Handbook of Concepts 2nd Edition*; Oxford: New York, 1994; ISBN 0198555733.

50. Weissman, S.I. Intramolecular Energy Transfer The Fluorescence of Complexes of Europium. *J. Chem. Phys.* **1942**, *10*, 214–217, doi:10.1063/1.1723709.

51. Sabbatini, N.; Guardigli, M.; Manet, I. Chapter 154 Antenna effect in encapsulation complexes of lanthanide ions. In *Handbook on the Physics and Chemistry of Rare Earths*; Elsevier, 1996; Vol. 23, pp. 69–119 ISBN 0168-1273.

52. Crosby, G.A.; Whan, R.E.; Alire, R.M. Intramolecular Energy Transfer in Rare Earth Chelates. Role of the Triplet State. *J. Chem. Phys.* **1961**, *34*, doi:https://doi.org/10.1063/1.1731670.

53. Crosby, G.A. Luminescent Organic Complexes of the Rare Earths. *Mol. Cryst.* **1966**, *1*, 37–81, doi:10.1080/15421406608083261.

54. Gutzov, S.; Berendts, S.; Lerch, M.; Geffert, C.; Börger, A.; Becker, K.D. High temperature optical spectroscopy investigations on Zr0.78Y0.18 Sm0.04O1.89 and Zr0.78 Y0.18 Ho0.04O1.89 single crystals. *Phys. Chem. Chem. Phys.* **2009**, *11*, 636–640.

55. Zahariev, T.; Shandurkov, D.; Gutzov, S.; Trendafilova, N.; Enseling, D.; Jüstel, T.; Georgieva, I. Phenanthroline chromophore as efficient antenna for Tb3+ green luminescence: A theoretical study. *Dye. Pigment.* **2020**, *185*, 108890.

56. Dexter, D.L. A Theory of Sensitized Luminescence in Solids. *J. Chem. Phys.* **1953**, *21*, 836–850, doi:10.1063/1.1699044.

57. Kawski, A.; Forster, V.T. Zwischenmolekulare Energiewanderung und Konzentrationsdepolarisation der Fluoreszenz. *Ann. Phys.* **1961**, *463*, 116–119, doi:10.1002/andp.19614630112.

58. Utochnikova, V. V. The use of luminescent spectroscopy to obtain information about the composition and the structure of lanthanide coordination compounds. *Coord. Chem. Rev.* **2019**, *398*, 113006.

59. Gaft, M.; Reisfeld, R.; Panczer, G. *Modern Luminescence Spectroscopy of Minerals and Materials*; Springer Berlin Heidelberg New York;

60. Binnemans, K. Interpretation of europium(III) spectra. *Coord. Chem. Rev.* **2015**, *295*, 1–45.

61. J. N. Demas; Crosby, G.A.; Demas, J.N. Measurement of Photoluminescence Quantum Yields. Review. *J. Phys. Chem.* **1971**, *75*, 991–1024, doi:doi:10.1021/j100678a001.

62. Porrès, L.; Holland, A.; Pålsson, L.-O.; Monkman, A.P.; Kemp, C.; Beeby, A.; Porres, L.; Holland, A.; Palsson, L.-O.; Monkman, A.P.; et al. Absolute Measurements of Photoluminescence Quantum Yields of Solutions Using an Integrating Sphere. *J. Fluoresc.* **2006**, *16*, 267–273, doi:DOI: 10.1007/s10895-005-0054-8.

63. Birks, J.B. *Photophysics of Aromatic Molecules*; Wiley-Interscience: London, 1970;

64. Williams, A.T.R.; Winfield, S.A.; Miller, J.N. Relative fluorescence quantum yields using a computer-controlled luminescence spectrometer. *Analyst* **1983**, *108*.

65. Pålsson, L.-O.; Monkman, A.P. Measurements of Solid-State Photoluminescence Quantum Yields of Films Using a Fluorimeter. *Adv. Mater.* **2002**, *14*, 757–758, doi:https://doi.org/10.1002/1521-4095(20020517)14:10<757::AID-ADMA757>3.0.CO;2-Y.

66. Greenham, N.C.; Samuel, I.D.W.; Hayes, G.R.; Phillips, R.T.; Kessener, Y.A.R.R.; Moratti, S.C.; Holmes, A.B.; Friend, R.H. Measurement of absolute photoluminescence quantum efficiencies in conjugated polymers. *Chem. Phys. Lett.* **1995**, *241*, 89–96, doi:https://doi.org/10.1016/0009-2614(95)00584-Q.

67. de Mello, J.C.; Wittmann, H.F.; Friend, R.H.; Mello, J.C. de; Wittmann, H.F.; Friend, R.H. An Improved Experimental Determination of External Photoluminescence Quantum Efficiency. *Adv. Mater.* **1997**, *9*, 230–232, doi:doi:10.1002/adma.19970090308.

68. Mersmann, A.B.; Scholl, S.E. *Fundamentals of Adsorption*; Am. Inst. Chem. Eng.: New York, 1991;

69. Gregg, S.J.; Sing, K.S.W. *Adsorption, Surface area and porosity*; Academic press, 1982;

70. Brunauer, S.; Deming, L.S.; Deming, W.E.; Teller, E. On a Theory of the van der Waals Adsorption of Gases. *J. Am. Chem. Soc.* **1940**, *62*, 1723–1732, doi:https://doi.org/10.1021/ja01864a025.

71. Halsey, G. Physical Adsorption on Non-Uniform Surfaces. *J. Chem. Phys.* **1948**, *16*, 931–937, doi:10.1063/1.1746689.

72. Haul, R. S. J. Gregg, K. S. W. Sing: *Adsorption, Surface Area and Porosity*. 2. Auflage, Academic Press, London 1982. 303 Seiten, Preis: $ 49.50. *Berichte der Bunsengesellschaft für Phys. Chemie* **1982**, *86*, 957, doi:10.1002/bbpc.19820861019.

73. Brinker, C.; Scherer, G. *Sol-gel science*; Academic press, 1990;

74. Saputra, R.E.; Astuti, Y.; Darmawan, A. Hydrophobicity of silica thin films: The deconvolution and interpretation by Fourier-transform infrared spectroscopy.

Spectrochim. Acta Part A Mol. Biomol. Spectrosc. **2018**, *199*, 12–20, doi:10.1016/j.saa.2018.03.037.

75. Lerot, L.; Low, P.F. Effect of swelling on the infrared absorption spectrum of montmorillonite. *Clays Clay Miner.* **1976**, *24*, 191–199.

76. Neimark, A.V. Determination of the surface fractal dimensionality from the results of an adsorption experiment. *Russ.J.Phys. Chem.* **1990**, *64*, 1397–1403.

77. Neimark, A. V. Calculating Surface Fractal Dimensions of Adsorbents. *Adsorpt. Sci. & Technol.* **1990**, *7*, 210–219, doi:10.1177/026361749000700402.

78. Sahouli, B.; Blacher, S.; Brouers, F. Applicability of the Fractal FHH Equation. *Langmuir* **1997**, *13*, 4391–4394, doi:10.1021/la962119k.

79. Neimark, A.V.; Ravikovitch, P.I. Capillary condensation in MMS and pore structure characterization. *Micropor. Mesopor. Mater* **2001**, *44/45*, 697–707.

80. Sing, K.S.W. Reporting physisorption data for gas/solid systems with special reference to the determination of surface area and porosity (Recommendations 1984). *Pure Appl. Chem.* **1985**, *57*, 603–619, doi:10.1351/pac198557040603.

81. Alothman, Z.A. A Review: Fundamental Aspects of Silicate Mesoporous Materials. *Materials (Basel).* **2012**, *5*, 2874–2902, doi:doi:10.3390/ma5122874.

82. Sing, K.S.W.; Everett, D.H.; Haul, R.A.W.; Moscoul, L.; Pierotti, R.A.; Rouquerol, J.; Seimieniewska, T. Reporting Physisorption Data for gas/Solid systems with Special Reference to the Determination of Surface Area and Porosity. *Pure Appl. Chem.* **1985**, *57*, 603—619.

83. Bhambhani, M.R.; Cutting, P.A.; Sing, K.S.W.; Turk, D.H. Analysis of nitrogen adsorption isotherms on porous and nonporous silicas by the BET and αs methods. *J. Colloid Interface Sci.* **1972**, *38*, 109–117, doi:10.1016/0021-9797(72)90226-3.

84. Gutzov, S.; Shandurkov, D.; Danchova, N.; Enseling, D.; Jüstel, T. Preparation and optical properties of functionalized hydrophobic aerogel granules. *SPIE Proc.* **2019**, *11332*, doi:10.1117/12.2552727.

85. Danchova, N.; Gutzov, S. Functionalization of Sol-Gel Zirconia Composites with Europium Complexes. *Z. Naturforsch* **2014**, *69*, 224 – 230.

86. Gutzov, S.; Shandurkov, D.; Danchova, N.; Petrov, V.; Spassov, T. Hybrid composites based on aerogels: preparation, structure and tunable luminescence. *J. Lumin.* **2022**, *251*, 119171.

87. Yadav, R.; Sardar, S.; Singh, M.; Mukherjee, R.K.; Anju; Singh, S.; Kushwaha, P.; Singh, S.P. Preparation of Holmium Oxide Solution as a Wavelength Calibration Standard for UV–Visible Spectrophotometer. *Mapan - J. Metrol. Soc. India* **2021**, *37*.

88. Georgieva, I.; Trendafilova, N.; Zahariev, T.; Danchova, N.; Gutzov, S. Theoretical insight

in highly luminescent properties of Eu(III) complex with phenanthroline. *J. Lumin.* **2018**, *202*, 192–205.

89. Shandurkov, D.; Danchova, N.; Spassov, T.; Petrov, V.; Gutzov, S. Luminescence of Binary-Doped Silica Aerogel Powders: A Two-Step Sol-Gel Approach. *Gels* **2024**, *10*, 104, doi:https://doi.org/10.3390/gels10020104.

90. Suzuki, K.; Kobayashi, A.; Kaneko, S.; Takehira, K.; Yoshihara, T.; Ishida, H.; Shiina, Y.; Oishi, S.; Tobita, S. Reevaluation of absolute luminescence quantum yields of standard solutions using a spectrometer with an integrating sphere and a back-thinned CCD detector. *Phys. Chem. Chem. Phys.* **2009**, *11*, 9850–9860, doi:10.1039/b912178a.

91. http://www.brucelindbloom.com CIE Color Calculator.

92. Hooda, A.; Khatkar, S.P.; Khatkar, A.; Malik, R.K.; Devi, S.; Dalal, J.; Taxak, V.B. Combustion synthesis, Judd–Ofelt parameters and optical properties of color tunable Ba3Y4O9: Eu3+ nanophosphor for near-UV based WLEDs. *J. Mater. Sci. Mater. Electron.* **2019**, *30*, 8751–8762.

93. Boruc, Z.; Fetlinski, B.; Kaczkan, M.; Turczynski, S.; Pawlak, D.; Malinowski, M. Temperature and concentration quenching of Tb3+ emissions in Y4Al2O9 crystals. *J. Alloys Compd.* **2012**, *532*, 92–97, doi:https://doi.org/10.1016/j.jallcom.2012.04.017.

94. Spectroscopic Properties of Rare Earths in Optical Materials. *Springer Ser. Mater. Sci.* 2005.

95. Schläfer, H.L.; Gliemann, G. *Basic Principles of Ligand Field Theory*; Wiley-Interscience: London, 1969; ISBN 0471761001.

96. Zahariev, T.; Trendafilova, N.; Georgieva, I. Spectroscopic and photophysical properties of [Eu(Phen)2]X3 (X≡Cl–, NO3–) complexes, incorporated into SiO2-based Matrices: Theoretical study. *Mater. Today Proc.* **2022**, *61*, 1292–1299.

97. Powdercell Available online: http://mill2.chem.ucl.ac.uk/ccp/web-mirrors/powdcell/a_v/v_1/powder/e_cell.html.

98. Meldrum, F.C.; O'Shaughnessy, C. Crystallization in Confinement. *Adv. Mater.* **2020**, *32*, 2001068, doi:DOI: 10.1002/adma.202001068.

99. Lindenberg, P.; Arana, L.R.; Mahnke, L.; Rönfeldt, P.; Heidenreich, N.; Doungmo, G.; Guignot, N.; Bean, R.; Chapman, H.; D.Dierksmeyer; et al. New insights into the crystallization of polymorphic materials:from real-time serial crystallography to luminescence analysis. *React. Chem. Eng.* **2019**, *4*, doi:DOI: 10.1039/C9RE00191C.